




Cite this: *Phys. Chem. Chem. Phys.*,
2024, 26, 27544

Modeling interfacial electric fields and the ethanol oxidation reaction at electrode surfaces†

Yuhan Mei,^a Fanglin Che^b and N. Aaron Deskins *^a

The electrochemical environment present at surfaces can have a large effect on intended applications. Such environments may occur, for instance, at battery or electrocatalyst surfaces. Solvent, co-adsorbates, and electrical field effects may strongly influence surface chemistry. Understanding these phenomena is an on-going area of research, especially in the realm of electrocatalysis. Herein, we modeled key steps in the ethanol oxidation reaction (EOR) over a common EOR catalyst, Rh(111), using density functional theory. We assessed how the presence of electrical fields may influence important C–C and C–H bond scission and C–O bond formation reactions with and without co-adsorbed water. We found that electric fields combined with the presence of water can significantly affect surface chemistry, including adsorption and reaction energies. Our results show that C–C scission (necessary for the complete oxidation of ethanol) is most likely through CH_xCO adsorbates. With no electric field or solvent present C–C scission of CHCO has the lowest reaction energy and dominates the oxidation of ethanol. But when applying strong negative fields (with or without solvent), the C–C scission of CH₂CO and CHCO becomes competitive. The current work provides insights into how electric fields and water solvent affect EOR, especially when simulated using density functional theory.

Received 12th July 2024,
Accepted 18th October 2024

DOI: 10.1039/d4cp02765e

rsc.li/pccp

1 Introduction

The growing demand for energy and the consumption of non-renewable fossil fuels have a negative impact on the environment. Fuel cells are widely regarded as a cleaner alternative energy technology. In particular, ethanol has attracted considerable interest as a fuel source due to its abundant availability from biomass feedstocks.^{1,2} Compared to other fuels, ethanol is also less toxic, has a higher boiling point, and possesses a high energy density comparable to that of gasoline.^{3–8} The complete ethanol oxidation reaction (EOR), which is ideal for maximizing electron production, involves efficient C–H and C–C bond cleavage leading to CO₂ as the final product.^{9–11} On the other hand, incomplete EOR involves hydrogen removal and potential C–O bond formation (while avoiding C–C scission), resulting in by-products such as acetaldehyde and acetic acid.^{12,13} Slow C–C bond scission (essential for complete EOR) at the anode catalyst (typically transition metals) limits the commercial viability of direct ethanol fuel cells (DEFCs). Since EOR occurs in an electrochemical environment, a thorough understanding of the relationship between surface chemistry and

reaction environment is critical to the scientific advancement of EOR catalysts.

Density functional theory (DFT) is a powerful tool for simulating electrochemical interfaces, which is the primary method used in the current study. There are various approaches to modeling electrochemical interfaces and describing the various components present at the interface (*e.g.*, solvent molecules, electric fields, electron potential, *etc.*).^{14–16} A common technique to account for the electrode potential is to simulate electrocatalytic hydrogen/electron transfer at metal surfaces by adding energy adjustments based on the electron potential at the electrode surface, also known as the computational hydrogen electrode (CHE) approach.¹⁷ However, the widely used CHE method overlooks the effects of electric fields present near the electrode surface. Such fields can significantly alter the surface chemistry and affect adsorbate interactions. Furthermore, C–C bond cleavage does not involve hydrogen/electron transfer, and thus the electric field and solvent molecules near the electrode surface are expected to influence C–C bond cleavage more than the potential of the electrons themselves. Other methods exist for modeling electrochemical systems, such as the computational standard hydrogen electrode (SHE)^{18,19} method, which determines redox potentials using *ab initio* molecular dynamics (AIMD). Such calculations can be time-consuming, and controlling local electric fields with this method can be difficult. A related method is the constant-potential hybrid-solvation dynamic model^{20,21} which also uses AIMD and requires varying

^a Department of Chemical Engineering, Worcester Polytechnic Institute, Worcester, Massachusetts 01609, USA. E-mail: nadeskins@wpi.edu

^b Department of Chemical Engineering, University of Massachusetts Lowell, Lowell, Massachusetts 01854, USA

† Electronic supplementary information (ESI) available. See DOI: <https://doi.org/10.1039/d4cp02765e>



the number of electrons added to or removed from the system to maintain a constant applied potential. One prominent method to simulate the electric fields present at electrochemical systems is to introduce a dipole sheet into the vacuum, which creates an electric field in the simulation cell.²²

Various DFT papers have examined the effect of an electrical field on surface chemistry.^{23–28} Electric fields can lead to remarkable behavior and variations in catalyst efficiency.^{23,24,29–34} It should be noted that it is possible to relate the electric field strength near the electrode surface to the electrode potential, as the electrode potential can be approximated as the double-layer thickness multiplied by the field strength, illustrated by Rossmelst *et al.*²³ A similar approach was used by Karlberg *et al.*³¹ Haruyama *et al.*³⁵ also developed methods to relate electric fields to the electrode potentials. In other DFT studies on the oxygen reduction reaction,^{24,31,36} electric fields were incorporated to improve the simulations. Electric fields were also included in studies of methane conversion.^{25,37,38} Estejab *et al.*³⁹ modeled methanol oxidation in the presence of an electric field. Regarding the study of electric fields in ethanol oxidation reactions, Jiang *et al.*²⁶ have used molecular dynamics simulations to investigate the effect of external electric fields of different strengths on EOR (albeit in the gas phase without the presence of a catalyst). Their study shows that the application of an electric field not only changes the reaction rate in a nonlinear manner, but also modifies the reaction pathways for ethanol oxidation.

Previous studies have used molecular modeling approaches to better understand the role of electric fields in C–C and C–H bond cleavage (important for many reactions involving organic species). Investigations by Che *et al.* examined the effect of electric fields on C–H bond cleavage of CH_x (x = 1–3) species over Ni,^{40,41} suggesting that negative external electric fields lower energy barriers while positive fields raise them. In recent work, Zhou *et al.*⁴² reported that for gas-phase pyrolysis of *n*-alkanes, electric fields can promote the breaking of C–C and C–H bonds. As for the C–C and C–H bond breakings in EOR, complementary studies using reactive force field (ReaxFF) molecular dynamics simulations have also been performed,^{26,27} analyzing the effects of external electric fields on the ethanol oxidation reaction mechanisms in the absence of a catalyst and in an O₂ gas environment. These modeling efforts suggest that electric fields can shift reaction mechanisms and possibly open alternative reaction pathways for oxidation of alcohols like ethanol. However, the precise influence of an external electric field on surface-mediated reactions relevant to complete ethanol oxidation, which involves the breaking of both C–C and C–H bonds, remains an open question in the context of DFT simulations.

In addition to electric fields present at electrocatalyst surfaces, solvent molecules can also alter catalyst reactivity. In particular, the solvation environment can be instrumental in facilitating various surface reactions, including both oxidation and electrocatalytic processes. Several studies focused on solvation effects and bond dissociation reactions on metal surfaces. Investigations by Schweitzer *et al.*⁴³ and Gu *et al.*⁴⁴ have shown that accounting for water solvation can significantly alter

the cleavage of C–C and C–H bonds in ethanol on a Pt(111) surface. Estejab *et al.* modeled methanol oxidation with explicit water molecules under an electric field. They indicated a dependency of both the solvation energy and the entropy on the strength and direction of an electric field, with the entropy of solvation being significantly impacted due to the orientation of water molecules.³⁹ Complementary findings by Mei *et al.*⁴⁵ highlighted the substantial role of a water solvent in modifying the dissociation of the C–C/C–H bonds on Rh(111). In a previous study, Guo *et al.*⁴⁶ used DFT coupled with an implicit continuum solvation model to investigate the potential-dependent mechanism of EOR on Pd. They proposed a mechanism where C–C bond scission changed only slightly under different potentials. In light of these previous findings, the current study aims to unravel the interactive effects of both the explicit presence of water and electric fields on EOR.

We investigated the influence of electric fields on EOR using DFT to model the Rh(111) surface, which has been previously recognized as an effective catalyst for EOR.^{7,10,47–53} We calculated the reaction energies for key EOR steps: C–C and C–H bond cleavage and C–O bond formation. Although there are numerous computational strategies for simulating electric fields,^{54–61} our approach was to apply an external electric field following the methodology established by Neugebauer and Scheffler,²² where a dipole sheet is inserted into the vacuum layer. Given that our focus is primarily on examining the effects of local electric fields, the dipole sheet method is both sufficient and computationally less expensive than other methods. Thus, we can simulate the effect of an electric field on adsorbate-covered surfaces. In addition, our study incorporated a co-adsorbed water molecule from the solvent environment to determine its effect on the EOR. The inclusion of explicit water molecules is a more representative model of solvation than implicit solvent models, especially in the context of relevant EOR processes.^{43,45,52,62,63} Previous work^{39,55,58} has demonstrated how electric fields can be used in conjunction with explicit water molecules to understand electrochemical interfaces. Our work extends this to better understand the role of the electrochemical environment on EOR.

2 Methodology

2.1 Computational details

Our DFT calculations used the Vienna *ab initio* Simulation Package (VASP).^{64–67} Core electrons were described using the projector augmented wave (PAW) method.^{68,69} The number of valence electrons simulated for each atom was 9 for Rh, 4 for C, 1 for H, and 6 for O. We performed tests on the number of valence electrons for Rh (9 or 15) in our previous work and the results indicated that 9 electrons was suitable for our modeling of Rh.⁴⁵ The Perdew–Burke–Ernzerhof (PBE) exchange–correlation functional⁷⁰ was used throughout the study. The plane wave basis was expanded to an energy cutoff of 400 eV. First order Methfessel–Paxton smearing⁷¹ with a smearing width of 0.1 eV was also used. The convergence criteria for the



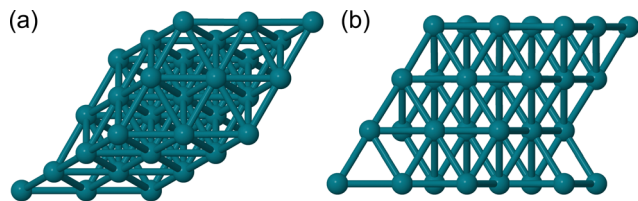


Fig. 1 The slab model used in this work to represent the Rh(111) surface: (a) top view and (b) side view. The slab was a (3×3) slab with four layers, the bottom two layers being frozen.

self-consistent field (SCF) energy calculations and atomic forces were set to 10^{-5} eV and 0.03 eV \AA^{-1} , respectively. All calculations in this study were spin-polarized. Bader charges were calculated with the code of Henkelman *et al.*^{72–74}

The Rh(111) surface was represented by a (3×3) four-layer slab (as shown in Fig. 1), with cell lengths of 8.15 \AA and a 10 \AA vacuum separation set in the z direction perpendicular to the surface. The bottom two layers of the slab were fixed. The lattice constant of bulk Rh was calculated to be 3.84 \AA , which is in agreement with previous work.^{9,10,51,75} For the slab calculations, a Gamma-centered k -point grid of $4 \times 4 \times 1$ was chosen to sample reciprocal space. Gas phase molecules were modeled in a 20 $\text{\AA} \times 20$ $\text{\AA} \times 20$ \AA box cell, and the gas phase calculations used a Monkhorst Pack k -point grid of $1 \times 1 \times 1$.

We modeled the adsorption of $\text{CH}_3\text{CH}_2\text{OH}$, $\text{CH}_3\text{CH}_2\text{O}$, $\text{CH}_2\text{CH}_2\text{O}$, CH_2OH , CH_2O , CH_3CO , CH_2CO , CHCO , CH_3 , CH_2 , CH , CO and H , as these species have been identified as key intermediates for the C–C and C–H bond breaking during ethanol oxidation/decomposition process.^{10,76,77} See also Fig. 2 for an illustration of various reactions and these species involved in EOR. In addition, we also modeled the adsorption of CH_3COOH , CH_3CO , and OH which are relevant for C–O bond formation. C–O bond formation can take place during incomplete EOR, and thus prevents complete EOR.^{12,13} Different initial geometries were considered in order to find stable configurations. Adsorbates were initially placed above the surface with atoms of the adsorbates at different fcc, hcp, top and bridge sites on the Rh(111) surface. The adsorption of larger molecules (*e.g.* $\text{CH}_3\text{CH}_2\text{OH}$, $\text{CH}_3\text{CH}_2\text{O}$, $\text{CH}_2\text{CH}_2\text{O}$, CH_3CO , CH_2CO , CHCO) can involve multiple interactions with the surface (*e.g.* $^*\text{CH}_3\text{CH}_2\text{OH}$ can have both of the C atoms interacting with Rh atoms). After geometry optimization, we took the structure with the lowest energy as the most stable configuration. For calculations in vacuum, geometries were first optimized without an external electric field, and then the most stable geometries were modeled in the presence of an external electric field in a range of -1.0 to 1.0 V \AA^{-1} , as discussed in the next section.

2.2 External electric field

An external electric field perpendicular to the metal slab was applied using the method of Neugebauer and Scheffler.²² This method is implemented in VASP, and has been used in previous studies.^{30,80–82} Fig. S1 (ESI[†]) illustrates this method. As discussed in previous studies,^{30,82,83} the Neugebauer and Scheffler method introduces an artificial dipole sheet in the

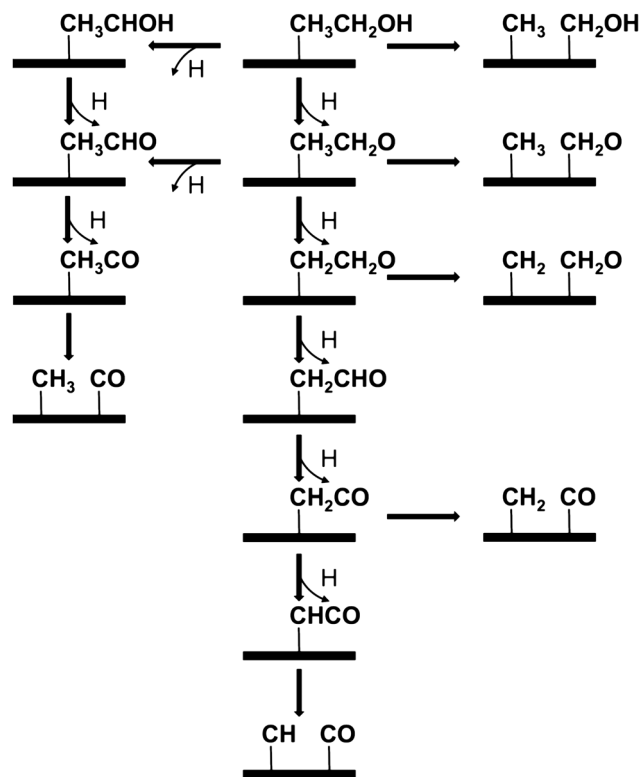


Fig. 2 Schematic representation of possible pathways for complete ethanol oxidation/decomposition on Rh(111).^{2,10,76,78,79} Key reactions involve C–C and C–H scission. Not shown are pathways for incomplete oxidation, leading to acetaldehyde, acetic acid, and possible other products. Further discussion of reactions modeled in this work is found in the Methodology section.

middle of the vacuum layer. We chose this method for its ability to assess the effects of local fields on surface chemistry, while remaining computationally efficient. The maximum electric field that can be introduced is limited by the height of the supercell due to “field emission” effects. An important requirement is to prevent the overlap between the electron density and the dipole sheet. Therefore, using the dipole sheet method requires a wide enough vacuum region. However, the vacuum must also not be too wide since a strong electric field will draw electrons out of the slab into the vacuum space and electrons may be found near the dipole sheet.^{30,83} Thus, in this work, applied electric fields had strengths up to ± 1 V \AA^{-1} .

Adsorption energies ($\Delta E_{\text{ads}}(F)$) were calculated using this equation:³⁰

$$\Delta E(F)_{\text{ads}} = E(F)_{\text{ads/slab}} - E(F)_{\text{slab}} - E(F)_{\text{ads(gas)}} \quad (1)$$

Here $E(F)_{\text{ads/slab}}$, $E(F)_{\text{slab}}$, and $E(F)_{\text{ads(gas)}}$ represent the total energy of a molecule adsorbed on the metal slab, the energy of the pure slab, and the energy of the gas phase adsorbate molecule. Energies were calculated at the applied field strength (F) for the gas-phase adsorbate, the bare slab, and the adsorbate-covered slab.

To determine the impact of the electric field on surface reactions, we modeled several C–C and C–H bond breaking and



C–O bond formation reactions over the Rh surface. We modeled C–C bond breaking involving $\text{CH}_3\text{CH}_2\text{OH}$, $\text{CH}_3\text{CH}_2\text{O}$, $\text{CH}_2\text{CH}_2\text{O}$, CH_3CO , CH_2CO , and CHCO . We also modeled C–H bond cleavage involving CH_3CO and CH_2CO . These reactions have been reported to be key reaction pathways in ethanol oxidation/decomposition.^{76,77,84,85} To calculate the reaction energies for C–C and C–H scission reactions (e.g., $\text{AB}^* \rightarrow \text{A}^* + \text{B}^*$), we used this formula:

$$\Delta E(F)_{\text{rxn}} = E(F)_{\text{A/slab}} + E(F)_{\text{B/slab}} - E(F)_{\text{AB/slab}} - E(F)_{\text{slab}} \quad (2)$$

$E(F)_{\text{A/slab}}$ and $E(F)_{\text{B/slab}}$ are the energies of species A and species B adsorbed on the metal surface. $E(F)_{\text{AB/slab}}$ represents the total energy of species AB adsorbed on the surface, while $E(F)_{\text{slab}}$ is the energy of the pure surface. All the energies in this equation were converged in the presence of an electric field (F). As for C–O bond formation, we modeled the reaction of acetic acid formation since acetic acid formation *via* the oxidation of adsorbed $\text{*CH}_3\text{CO}$ by *OH species is one of the main side reactions in ethanol oxidation.^{86–89} Inhibiting C–O bond formation is essential for complete ethanol oxidation. To calculate these reaction energies, we used a similar formula as eqn (2), except the product was adsorbed acetic acid while the reactants were adsorbed CH_3CO and OH .

2.3 Effect of water

To more fully evaluate the impact of the electrochemical environment on surface chemistry, co-adsorbed water was included in some simulations. We added a water molecule to interact with the surface species, and a similar approach to account for solvation effects was used by others.^{43,90,91} With the addition of the water molecule, determining the most stable geometries becomes more complicated. We considered various possible arrangements of the water molecules relative to the adsorbate. Several initial geometries were chosen, similar to our previous work.⁴⁵ However, we used two distinct methods to further select the initial geometries. In the first method, four unique geometries (see Fig. S2, ESI† for an example with ethanol) for each adsorbate + water combination were first optimized without an external electric field, and then the most stable geometry of these potential-free calculations was used as the initial geometry in the presence of an electric field. Thus, only one initial geometry was used for the calculations in the presence of an electric field. In principle, this method should save time and has been used before.^{30,40,41} In the second method, we modeled four different initial geometries at each potential. These initial geometries may be different from the potential-free geometries and thus may lead to new optimized structures in the presence of an electric field. This method requires more calculations in the presence of an electric field, and such calculations may have more difficulty converging compared to calculations without an electric field. Thus, the second method may be more time-consuming, but may find stable geometries that our first method did not find. We simply refer to these as Method 1 and Method 2 in the text. Further details on these methods can be found in the ESI,† as well as an illustration of these two methods (see Fig. S3, ESI†). As we discuss further in the paper,

different results can be obtained depending on the method of initial geometries chosen.

We compared adsorption energies and reaction energies in vacuum (no water present) with results using explicit water. We also evaluated field effects by modeling solvated structures with applied electric fields. For these calculations, the adsorption energies were calculated with the following:^{92,93}

$$\Delta E(F)_{\text{ads}}^{\text{sol}} = E(F)_{(\text{ads}+\text{H}_2\text{O})/\text{slab}} - E(F)_{\text{H}_2\text{O}/\text{slab}} - E(F)_{\text{ads}(\text{gas})} \quad (3)$$

Here $E(F)_{(\text{ads}+\text{H}_2\text{O})/\text{slab}}$, $E(F)_{\text{H}_2\text{O}/\text{slab}}$, and $E(F)_{\text{ads}(\text{gas})}$ represent the total energy of a molecule adsorbed on the metal slab in the presence of water, the energy of the water adsorbed on the metal slab, and the energy of the gas phase adsorbate molecule, respectively. All these energies were calculated in the applied field (F). The reaction energies for bond cleavage (e.g., $\text{AB}^* \rightarrow \text{A}^* + \text{B}^*$) with water were calculated with this equation:^{93,94}

$$\Delta E(F)_{\text{rxn}}^{\text{sol}} = E(F)_{(\text{A}+\text{H}_2\text{O})/\text{slab}} + E(F)_{(\text{B}+\text{H}_2\text{O})/\text{slab}} - E(F)_{(\text{AB}+\text{H}_2\text{O})/\text{slab}} - E(F)_{\text{H}_2\text{O}/\text{slab}} \quad (4)$$

We acknowledge that all our calculated energies do not include entropic effects. Entropy values can be calculated, for instance using molecular dynamics simulations and are not trivial to calculate.^{39,95} Future work may include these effects.

3 Results and discussion

In this section, we report on the influence of electric fields on the adsorption of species relevant to ethanol oxidation. Additionally, we investigate the impact of electric fields on the reactivity of C–C and C–H bond cleavage, both of which are relevant to ethanol oxidation. Finally, we explore the interplay between electric fields and the presence of water in ethanol oxidation.

3.1 Effect of an electric field on adsorption

During ethanol oxidation, many reaction steps (e.g., C–C bond cleavage, dehydrogenation, C–O formation) are possible, as shown in Fig. 2. The reactivity of reaction species is influenced by their stability. Therefore, we have modeled the adsorption of several key intermediates. C–C cleavage plays a crucial role in complete oxidation and can occur through several intermediates, including $\text{CH}_3\text{CH}_2\text{OH}$, $\text{CH}_3\text{CH}_2\text{O}$, $\text{CH}_2\text{CH}_2\text{O}$, CH_3CO , CH_2CO , and CHCO .^{10,76,77,96} Consequently, we have modeled the adsorption of the following species: $\text{CH}_3\text{CH}_2\text{OH}$, $\text{CH}_3\text{CH}_2\text{O}$, $\text{CH}_2\text{CH}_2\text{O}$, CH_2OH , CH_2O , CH_3CO , CH_2CO , CHCO , CH_3 , CH_2 , CH , CO , and H . The adsorption energies of selected species without an applied field were calculated and compared with previously reported literature values,^{9,10,52} as shown in Table S1 (ESI†). Our calculated energies were in good agreement with the literature values, thus validating our computational approach.

We present the adsorption energies in the presence of an electric field for selected species in Fig. 3. The adsorption energies in the presence of an electric field for 15 different species are shown in Fig. S4 (ESI†). Analysis of the data from



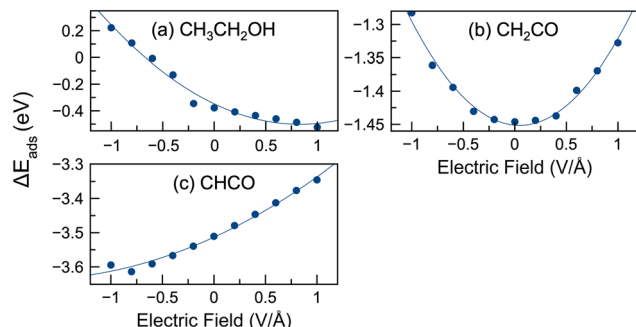


Fig. 3 Adsorption energies of select species in the presence of electric fields. All calculations were for lone adsorbates (no water present). Three different adsorption curve patterns were observed in this work. Shown is an example of (a) negative slope (ethanol), (b) parabolic shape (CH_2CO), and (c) positive slope (CHCO).

Fig. 3 and Fig. S4 (ESI[†]) reveals three distinct patterns of behavior. The first group of species (including $\text{CH}_3\text{CH}_2\text{OH}$, $\text{CH}_3\text{CH}_2\text{O}$, $\text{CH}_2\text{CH}_2\text{O}$, CH_2OH , CH_3CO , CH_3 , CH_2 , CH_3COOH , and OH) exhibited a decrease in adsorption energies with increasing field strength (*i.e.*, became more stable) or a negative slope in the adsorption energy *versus* electric field plot. In contrast, the second group of species (CHCO and CO) showed an increase in adsorption energies with increasing field strength, reflecting a positive slope in the adsorption energy *versus* the electric field profile. The third group of species (CH_2O , CH, CH_2CO , and H) showed a parabolic trend, with adsorption energies initially decreasing before reaching a minimum and then increasing. Notably, in the case of the parabolic plots, the adsorption energies of CH_2O and CH reached their lowest values at slightly positive potentials, while the adsorption energies of CH_2CO and H reached their minimum at or near $0 \text{ V } \text{Å}^{-1}$. It should be noted that while we have identified three different patterns in these plots, those curves with positive or negative slope display curvature, such that parabolic behavior may be observed at much lower or larger potentials (well beyond -1 or $1 \text{ V } \text{Å}^{-1}$).

Upon applying the electric fields, the optimized geometries of the adsorbates underwent only minor changes, with an example shown in Fig. S5 (ESI[†]). Changes in bond lengths within the adsorbates were less than 0.04 Å for all species studied when applying the electric field. In addition, we evaluated the structural fluxionality of these adsorbates following a similar approach discussed by Yang *et al.*,⁹⁷ as described in the ESI[†]. This approach facilitated the comparison of adsorbate/surface geometries under electric fields with those without electric fields. The calculated structural fluxionality values, shown in Table S2 (ESI[†]), revealed negligible changes in geometry due to the electric fields. For example, the highest observed fluxionality value was only 0.02 Å for CH_2OH at an electric field strength of $1 \text{ V } \text{Å}^{-1}$.

In our study, we have investigated the variations of adsorbate–surface distances under different electrical potentials. Most of the adsorbates studied, such as $\text{CH}_3\text{CH}_2\text{OH}$, $\text{CH}_3\text{CH}_2\text{O}$, $\text{CH}_2\text{CH}_2\text{O}$, CH_2OH , CH_2O , CH_2O , CH_2O , CH_2O , CH_2O , CH_2O ,

CH_2O , CH_2O , CH_3CO , CH_2CO , CH_3 , and OH , bonded to the surface mainly through Rh–O and Rh–C interactions. Our results showed that positive electric fields generally decreased the distances between these adsorbates and the surface, with Rh–O and Rh–C bond lengths shortened by up to 0.20 Å . Conversely, negative electric fields increased the distances. This phenomenon can be attributed to the polarization of the metal surfaces in a positive electric field, which induces a partial positive charge, increasing the attraction to negatively charged O atoms *via* electrostatic forces, as supported by the literature.^{30,41} Notably, CHCO and CO species also adsorbed through Rh–C bonds, while showing minimal distance reduction (0.03 Å) under negative potentials. In contrast, the distances for adsorbed CH_2 , CH and H atoms remained relatively unchanged, with bond length variations of only up to 0.01 Å . Thus, the most significant distance changes occurred for negatively charged adsorbates such as O at positive potentials, while other adsorbate distances were less affected by the applied potentials. Our results are consistent with previous studies. For example, the H adsorption energies, which increase at both positive and negative potentials, agree with the results of Che *et al.*⁴⁰ on their investigations involving Ni(111) surfaces. This congruence extends to other species in their work as well; the adsorption energy profile of CH shows a parabolic shape, reaching optimal stability at a modest positive potential. In contrast, the adsorption energies for CH_2 and CH_3 show a monotonic decrease with increasing potential. The adsorption energy of CO, on the other hand, shows an upward trend with increasing potential, a trend that is also in good agreement with the findings of Che *et al.*,⁴¹ further validating our results by aligning with the established literature.

Fig. 3 illustrates the possible significant influence of an external electric field on the adsorption energies of reactive intermediates. The difference in adsorption energies between $1 \text{ V } \text{Å}^{-1}$ and $-1 \text{ V } \text{Å}^{-1}$ reached up to 1 eV , with an average variation across these species of 0.44 eV . Our study also investigated the variation of adsorption energies under different potentials compared to the baseline ($0 \text{ V } \text{Å}^{-1}$), denoted as $|E(0)_{\text{ads}}| - |E(\vec{F})_{\text{ads}}|$. The maximum variance was observed for ethanol, with a value of 0.60 eV at $-1 \text{ V } \text{Å}^{-1}$. In Fig. 3 the largest deviations were typically observed at -1 or $1 \text{ V } \text{Å}^{-1}$. The average maximum variance for all species was 0.29 eV . Some species showed significant deviations from $0 \text{ V } \text{Å}^{-1}$ (*e.g.* ethanol, $\text{CH}_3\text{CH}_2\text{O}$, CH_3COOH , OH), while others have smaller deviations (*e.g.* CH_2CO , CHCO, CH_2). For example, the adsorption energy range of CH_2CO was 0.16 eV , suggesting a more limited influence of the electric potential on its adsorption.

In general, the application of a positive electric field resulted in a decrease of the adsorption energies for most of the intermediates. However, exceptions were observed for CH_2CO , CH_2O , CHCO, CH, CO, and H, where the adsorption energies increased in positive electric fields. This suggests that positive electric fields can stabilize many species on the surface, whereas negative fields tend to destabilize them. The implications of these field effects on the reaction energies of the steps involved in EOR are discussed later in the paper.



3.2 Dipole moments and polarizability analysis

As discussed in previous studies,^{30,40,41,82,98,99} dipole moments and polarizabilities can be derived from the relationship between adsorption energies and the magnitude of the local electric field. If we know the effective dipole moment and the effective polarizability, we can predict how electric field vectors with the dipole moments affect the adsorption energy of adsorbates on metal surfaces at several different potentials. The adsorption energies can be written in terms of a Taylor series expansion:

$$\Delta E(\vec{F})_{\text{ads}} \approx E(\vec{F} = 0)_{\text{ads}} - \vec{\mu} \cdot \vec{F} - \frac{1}{2}\alpha F^2. \quad (5)$$

Here $E(\vec{F} = 0)_{\text{ads}}$ is the adsorption energy in the absence of the electric field. $\vec{\mu}$ and α are defined as the effective dipole moment and polarizability evaluated at the zero electric field and can be fitted from the data. The values of $\vec{\mu}$ and α are also the first and second derivatives of the field-dependent adsorption energies and are listed in Table 1. Fig. 3 shows the effects of electric fields on the adsorption energies of different species discussed in Section 3.1. The first group of species ($\text{CH}_3\text{CH}_2\text{OH}$, $\text{CH}_3\text{CH}_2\text{O}$, $\text{CH}_2\text{CH}_2\text{O}$, CH_2OH , CH_3CO , CH_3 , CH_2 , CH_3COOH , and OH) experience an increase in adsorption energy under negative electric fields and a decrease under positive electric fields, which correlates with their positive effective dipole moments as listed in Table 1. Conversely, species such as CHCO and CO , which have negative effective dipole moments, show increased adsorption energies with increasing electric field strength. For CH_2O and CH , which have small positive effective dipole moments ($<0.1 \text{ eV \AA}^{-1} \text{ V}^{-1}$), the adsorption energies increase for both strong negative and strong positive electric fields, but decrease for weak positive fields. Similarly, for species such as CH_2CO and H with near-zero effective dipole moments, both negative and positive electric fields increase their adsorption energies. These results confirm that the effect of electric fields on adsorption energies is significantly influenced by the magnitude

of the effective dipole moments of the species, with pronounced field effects corresponding to stronger effective dipole moments.⁴¹ The calculated results presented in Table 1 are in agreement with previous research⁴¹ on species such as CH_2OH , CH_2O , CH_3 , CH_2 , CH , CO , H , and OH . This previous research focused on $\text{Ni}(111)$ surfaces, which may explain any observed differences between our results and theirs.

3.3 Bader charge analysis

We also performed Bader charge analysis, summarized in Table 2 and illustrated in Fig. S6 (ESI[†]). This analysis focused on species under vacuum in order to elucidate more details how fields change adsorbate properties. It was observed that Bader charges generally decreased with increasing electric field, which was consistent with trends observed in previous studies on the Ni surface.⁴¹ The first set of species identified in Section 3.1 (including $\text{CH}_3\text{CH}_2\text{OH}$, $\text{CH}_3\text{CH}_2\text{O}$, $\text{CH}_2\text{CH}_2\text{O}$, CH_2OH , CH_3CO , CH_3 , CH_2 , CH_3COOH , and OH) showed consistent trends in their adsorption energies. In particular, negative electric fields were found to weaken the adsorption, while positive electric fields enhanced it. These trends in adsorption energies were correlated with Bader charges. As shown in Fig. S6 (ESI[†]), Rh atoms bound to these intermediates were predominantly positively charged (except for CH_3COOH and OH), and their charges increased as the electric field shifted from negative to positive. This increase in positive charge on Rh atoms increased their attraction to the negatively charged C and O atoms in the adsorbed species, resulting in stronger adsorption under positive electric fields. For CH_3COOH , adsorption occurred through the O–Rh interaction, with both O and Rh atoms initially negatively charged. Therefore, adsorption became stronger as Rh atoms became less negatively charged under positive electric fields. Similarly, OH adsorption on Rh surfaces involves O–Rh bonding, where O atoms were negatively charged, and Rh atoms became more positively charged under positive electric fields, thus strengthening a O–Rh interaction.

We show in Fig. S7 (ESI[†]) a comparison of the adsorption energies and Bader charges of Rh atoms, which illustrates how adsorption energies of species bonding through negative atoms become stronger as Rh atoms become more positively charged. For species with positive effective dipole moments (such as $\text{CH}_3\text{CH}_2\text{OH}$, $\text{CH}_3\text{CH}_2\text{O}$, $\text{CH}_2\text{CH}_2\text{O}$, CH_2OH , CH_3CO , CH_3 , CH_2 , CH_3COOH , and OH) negative electric fields weaken adsorption, while positive fields strengthen adsorption. Because more positive charges on Rh atoms (under positive fields) increases their attraction to negatively charged C and O atoms, adsorption is strengthened. Similarly, less positive charges (under negative fields) weaken adsorption. Species with negative effective dipole moments, such as CHCO and CO , show weaker binding under positive electric fields due to increased positive charge on both Rh and C atoms, resulting in decreased adsorption. For species with small effective dipole moments, such as CH_2CO , CH , and H , there is a more complex relationship between Rh charges and charges of the adsorbate.

The second group of species, CHCO and CO , was found to adsorb onto the Rh surfaces *via* interactions involving both C

Table 1 The effective dipole moments (in units of $\text{eV \AA}^{-1} \text{ V}^{-1}$) and polarizabilities (in units of $\text{eV \AA}^2 \text{ V}^{-2}$) of several adsorbates as calculated from a Taylor series expansion of the adsorption energies as a function of the electric field

	This work		Literature	
	$ \vec{\mu} $	α	$ \vec{\mu} $	α
* $\text{CH}_3\text{CH}_2\text{OH}$	0.37	−0.44		
* $\text{CH}_3\text{CH}_2\text{O}$	0.33	−0.17		
* $\text{CH}_2\text{CH}_2\text{O}$	0.20	−0.18		
* CH_2OH	0.22	−0.03	0.16 ⁴¹	−0.93 ⁴¹
* CH_2O	0.09	−0.16	0.30 ⁴¹	0.00 ⁴¹
* CH_3CO	0.23	−0.14		
* CH_2CO	0.01	−0.29		
* CHCO	−0.14	−0.08		
* CH_3	0.19	−0.11	0.19; ⁴¹ 0.19 ⁴⁰	−0.02; ⁴¹ −0.15 ⁴⁰
* CH_2	0.13	−0.12	0.14; ⁴¹ 0.14 ⁴⁰	−0.02; ⁴¹ −0.16 ⁴⁰
* CH	0.08	−0.19	0.08; ⁴¹ 0.08 ⁴⁰	−0.19; ⁴¹ −0.19 ⁴⁰
* CO	−0.22	−0.09	−0.21 ⁴¹	−0.06 ⁴¹
* H	−0.01	−0.06	−0.01; ⁴¹ −0.01 ⁴⁰	−0.03; ⁴¹ −0.06 ⁴⁰
* CH_3COOH	0.47	−0.05		
* OH	0.56	0.00	−0.09 ⁴¹	−0.05 ⁴¹



Table 2 Calculated Bader charges of different intermediates using different solvation methods and applied fields. The numbers in each column represent the Bader charges of the adsorbed species in a negative electric field (-1 V \AA^{-1}), no electric field (0 V \AA^{-1}), and in a positive electric field (1 V \AA^{-1})

Species	Vacuum	Solvation method 1	Solvation method 2
*CH ₃ CH ₂ OH	-0.15/0.03/0.04	-0.05/0.00/-0.01	0.40/-0.03/0.00
*CH ₃ CH ₂ O	-0.59/-0.40/-0.38	-0.69/-0.46/-0.45	-0.68/-0.43/-0.49
*CH ₂ CH ₂ O	-0.71/-0.51/-0.36	-0.81/-0.63/-0.53	-0.71/-0.57/-0.73
*CH ₂ OH	-0.24/-0.06/0.06	-0.28/-0.13/-0.04	-0.34/-0.13/-0.14
*CH ₂ O	-0.58/-0.40/-0.27	-0.49/-0.46/-0.36	-0.94/-0.52/-0.41
*CH ₃ CO	-0.37/-0.17/-0.09	-0.44/-0.28/-0.24	-0.54/-0.28/-0.35
*CH ₂ CO	-0.60/-0.40/-0.24	-0.71/-0.55/-0.41	-0.87/-0.55/-0.66
*CHCO	-0.47/-0.31/-0.13	-0.63/-0.50/-0.35	-0.69/-0.50/-0.84
*CH ₃	-0.35/-0.18/-0.09	-0.22/-0.20/-0.12	-0.52/-0.20/-0.09
*CH ₂	-0.44/-0.27/-0.18	-0.30/-0.27/-0.21	-0.78/-0.27/-0.71
*CH	-0.42/-0.27/-0.20	-0.30/-0.32/-0.26	-1.48/-0.32/-0.23
*CO	-0.42/-0.30/-0.20	-0.51/-0.43/-0.34	-0.63/-0.43/-0.15
*H	-0.25/-0.16/-0.14	-0.17/-0.18/-0.16	-0.19/-0.18/-0.15
*CH ₃ COOH	-0.21/0.00/0.02	-0.11/-0.08/-0.07	-0.60/-0.07/-0.31
*OH	-0.63/-0.46/-0.40	-0.55/-0.48/-0.44	-0.59/-0.48/-0.47

atoms in CHCO and the C atom in CO, forming Rh–C bonds. The Rh atoms in these interactions were positively charged. In CHCO, one of the carbon atoms was positively charged and the other was negatively charged, as shown in Fig. S6 (ESI[†]). As the electric fields shift from negative to positive, the positively charged carbon atoms in CHCO became more positively charged, while the negatively charged carbon atoms became less negatively charged. This change results in increased repulsion or decreased attraction between the Rh and carbon atoms, leading to weaker adsorption in positive electric fields. Similarly, CO molecules bonded to the Rh surface through C–Rh bonds, where both the Rh and carbon atoms were positively charged. Therefore, in positive electric fields, the repulsion or weaker bonding between the Rh and carbon atoms was increased, reducing the strength of the adsorption. Indeed, Fig. S7 (ESI[†]) again shows that for these species more positive Rh atoms correlates with weaker adsorption.

The third set of species, including CH₂O, CH₂CO, CH and H, showed adsorption characteristics different from the previous two groups, having parabolic adsorption curves (see Fig. 3 and Fig. S4, ESI[†]). CH₂O and CH species bound to the surface through Rh–O and Rh–C bonds, respectively, while CH and H bound through Rh–C and Rh–H bonds, respectively. In CH₂O and CH₂CO, O atoms were negatively charged while carbon atoms were positively charged. Rh atoms bound to CH₂O and CH₂CO were positively charged. In positive electric fields, the charges on the oxygen atoms decreased, reducing the attraction between the negatively charged oxygen and the positively charged Rh. Conversely, in negative fields, the Rh atoms bound to oxygen became less positively charged, weakening the Rh–O bond. Thus, electric fields modulated the charges and interactions between oxygen and Rh atoms, affecting the adsorption energy profiles of CH₂O and CH₂CO. For CH, the carbon atom exhibited reduced negative charge in both negative and positive fields. This weakened the interaction between negatively charged carbon and positively charged Rh as reflected in the adsorption energy behavior of CH. Adsorbed H atoms were always negative upon adsorption, and in negative fields, negatively charged Rh atoms decrease the Rh–H interaction,

while in positive fields, despite Rh being more positively charged, the reduced charge on H led to weaker adsorption. We note that similar negative charges for H interacting with metals were observed by others.^{100–102} Overall, the Bader charge analysis elucidates how external electric fields significantly influence charge transfer and ionic interactions between adsorbates and metal surfaces, altering the adsorption behavior of various intermediates.

3.4 Effect of an electric field on reactivity

Our results also show that an electric field can affect the cleavage of C–C/C–H bonds in species relevant to EOR. Calculated reaction energies for C–C bond cleavage reactions are shown in Fig. 4. There are several interesting trends. Some reaction curves were parabolic (*i.e.* CH₃CH₂OH, CH₃CH₂O, CH₂CH₂O, CHCO), while others were more linear (*i.e.* CH₃CO and CH₂CO). The application of negative electric fields was found to facilitate C–C bond dissociation by reducing the reaction energies in CH₃CO, CH₂CO, and, to a lesser extent, CH₃CH₂O. In contrast, the addition of positive electric fields resulted in increased reaction energies in most of the C–C bond cleavage reactions studied, although with a slight reduction in the case of CH₃CH₂OH. This phenomenon of increased reaction energies under positive electric fields could be attributed to increased adsorption energies of the reactant species (*i.e.*, more stable reactants) and/or decreased adsorption energies of product species (*i.e.*, less stable products), as discussed in the previous section. We do note, however, that the changes in reaction energies across the different potentials are mostly small, typically less than 0.1 eV. Exceptions are CH₃CO and CH₂CO, where the reaction energies vary by 0.5 eV (CH₃CO) and 0.25 eV (CH₂CO) from -1 to 1 V \AA^{-1} . Of note, CH_xCO species are generally the most favorable for C–C scission, and therefore key reaction species.^{76,77,103–105} Thus, an electric field had little effect on the reaction energies, except for selected species in which more negative potentials favored C–C scission.

For C–H bond cleavage, as shown in Fig. 5, both the reaction energies of CH₃CO and CH₂CO increased with increasing potential. The reaction energies increased by 0.37 and 0.38 eV



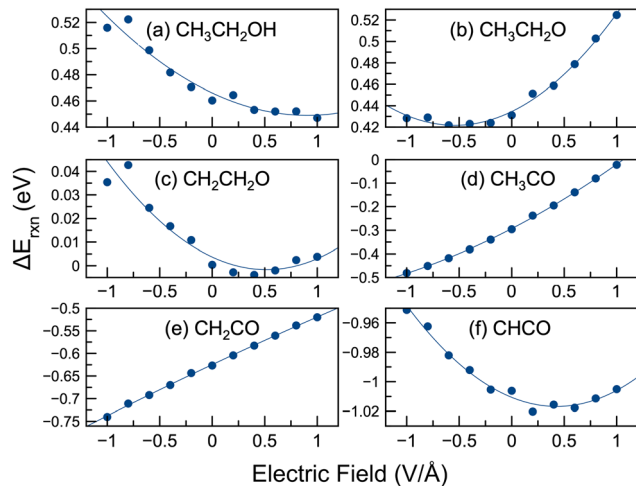


Fig. 4 Reaction energies for C–C bond breaking in the presence of external electric fields in the vacuum phase. Reactions modeled: (a) $\text{CH}_3\text{CH}_2\text{OH} \rightarrow \text{CH}_3 + \text{CH}_2\text{OH}$; (b) $\text{CH}_3\text{CH}_2\text{O} \rightarrow \text{CH}_3 + \text{CH}_2\text{O}$; (c) $\text{CH}_2\text{CH}_2\text{O} \rightarrow \text{CH}_2 + \text{CH}_2\text{O}$; (d) $\text{CH}_3\text{CO} \rightarrow \text{CH}_3 + \text{CO}$; (e) $\text{CH}_2\text{CO} \rightarrow \text{CH}_2 + \text{CO}$; (f) $\text{CHCO} \rightarrow \text{CH} + \text{CO}$.

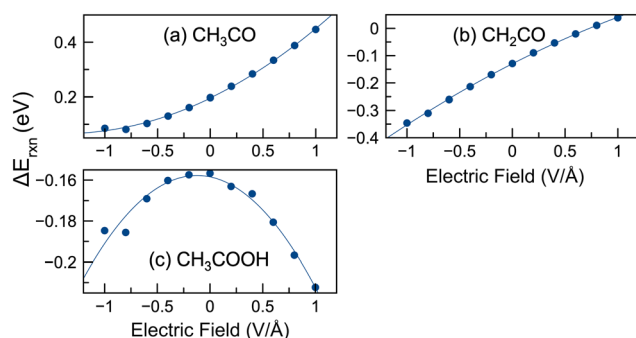


Fig. 5 Reaction energies for C–H bond breaking in the presence of external electric fields in the vacuum phase, as well as C–O formation. Reactions modeled: (a) $\text{CH}_3\text{CO} \rightarrow \text{CH}_2\text{CO} + \text{H}$; (b) $\text{CH}_2\text{CO} \rightarrow \text{CHCO} + \text{H}$; (c) $\text{CH}_3\text{CO} + \text{OH} \rightarrow \text{CH}_3\text{COOH}$.

for CH_3CO and CH_2CO , respectively, between -1 V \AA^{-1} and 1 V \AA^{-1} . C–O bond formation in an electric field was more complicated. The results show that both negative and positive potentials favored C–O formation. In negative electric fields, the reaction energy decreased by up to 0.029 eV, while in positive electric fields, the reaction energy decreased by up to 0.056 eV. Thus, negative potentials favored the C–H bond cleavage and C–O bond formation reactions in EOR, while positive potentials favored only C–O bond formation. However, the effect of a potential on C–O formation was rather small.

Our results indicate that the presence of an external electric field has a significant effect on the reaction energies for selected C–C/C–H bond cleavage and C–O bond formation reactions. Negative electric fields could significantly lower the reaction energies of certain C–C and C–H bond cleavages. On the other hand, positive electric fields had minimal effect in lowering the reaction energies and significantly increased the reaction energies for some species. Both negative and positive

electric fields favored the formation of the C–O bond, although the effect was small. Therefore, it appears that negative electric fields are likely to have the most beneficial effect in increasing the rate of the EOR reaction steps, at least in the absence of water. This finding correlates well with the experimental results that ethanol decomposes on Rh surfaces at negative onset potentials *via* C–H bond cleavage to form intermediates such as acetic acid and acetaldehyde, and C–C bond cleavage to form CO or CO_2 .^{106–109}

3.5 Effect of an electric field and co-adsorbed water on adsorption

Liquid–metal interfaces occur in many electrochemical systems, such as batteries, electrolytic cells, and fuel cells.²⁹ Therefore, in addition to electrical potentials, we also considered the effect of water on Rh surface chemistry. The inclusion of a solvent, such as water, can significantly affect surface reactions.^{43–45,110–112} Previous work has shown that explicit solvation methods that directly include solvent molecules as part of the simulation can accurately describe solvation effects resulting from hydrogen bonding between adsorbates and solvents.^{52,92,93,113–117} In our work,⁴⁵ we have also shown that the inclusion of explicit water and ethanol solvent molecules can greatly affect C–C/C–H bond cleavage and C–O formation in ethanol oxidation reactions, more so than implicit solvation approaches. Explicit water–metal interfaces in the presence of external electric fields have also been studied in previous work.^{39,55,58} In our work, we modeled surfaces where an additional water molecule was added to the system. A similar approach of using a water molecule as a proxy for the solvent has been used previously.^{43,90,91} Thus, the adsorption and reaction energies in the presence of electric fields and water were calculated.

In Fig. 6 we show the adsorption energies of selected species in the presence of an electric field and water. Fig. S10 (ESI[†]) shows similar adsorption energies for 15 different species. Unlike the vacuum calculations, the adsorption energy–potential plots for most species are parabolic, increasing with increasing/decreasing potential. Exceptions are CH_3COOH and OH, which have negative slopes. The lowest adsorption energies do not always occur at 0 V \AA^{-1} , but can occur at weak positive potentials ($\text{CH}_3\text{CH}_2\text{O}$, $\text{CH}_2\text{CH}_2\text{O}$, CH_2OH , CH_3CO , and CH_2) or weak negative potentials (CHCO , CO). Some species had their lowest adsorption energies near 0 V \AA^{-1} ($\text{CH}_3\text{CH}_2\text{OH}$, CH_2O , CH_2CO , CH_3 , CH, and H). In the case of CO, a recent paper³⁹ showed favorable interactions between water and CO at moderately negative potentials. We observed a similar effect where CO adsorption energies with water also decreased at moderate negative potentials.

In this study, as discussed in Section 2, we started with different initial geometries at 0 V \AA^{-1} and chose the most stable structures as the initial geometries for further calculations in electric fields (*i.e.* Method 1). When we started with several possible initial geometries and then applied an electric field (*i.e.* Method 2), the adsorption energies, as shown in Fig. 6, could be quite different for some species. In general, the



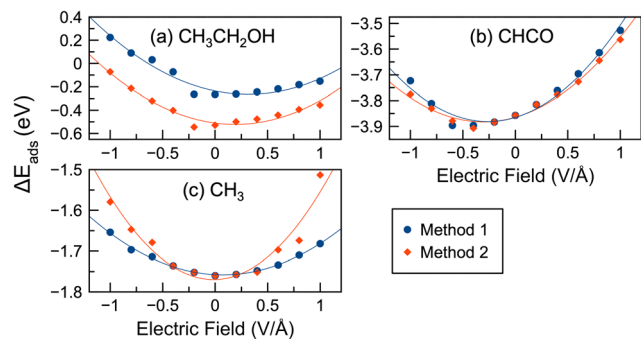


Fig. 6 Adsorption energies of select species under an electric field and with water present. Two different approaches (Method 1 and 2 as discussed in the Methodology) were used for selecting initial geometries for the optimizations. Shown are three different types of situations: (a) Method 2 had lower energies than Method 1 ($\text{CH}_3\text{CH}_2\text{OH}$); (b) Methods 1 and 2 have almost identical energies (CHCO); or (c) Methods 1 and 2 give similar energies, but with some deviations (CH_3).

adsorption energies using Method 2 followed a trend similar to that of Method 1, but the adsorption energies decreased by -0.04 eV on average. The highest increases and decreases in adsorption energy were 0.17 eV (CH_3 at 1.0 V \AA^{-1}) and 0.35 eV ($\text{CH}_3\text{CH}_2\text{OH}$ at -0.6 V \AA^{-1}), respectively. CH_2O also had significantly lower adsorption energies with Method 2 compared to Method 1 by an average of 0.12 eV. Fig. 6 shows that the differences in adsorption energies between Methods 1 and 2

are often most pronounced at larger potentials (e.g. near 1 V \AA^{-1} or -1 V \AA^{-1}): CH , OH , CH_3 , CH_2 , $\text{CH}_2\text{CH}_2\text{O}$, etc.

We discuss a specific example of how the optimization approach affects the final geometries. Fig. 7 and Section 7 of the ESI† both provide details on the geometries of $\text{CH}_3\text{CH}_2\text{O}$ using Methods 1 and 2. When using both Method 1 and Method 2, the orientation of the water molecule adopts one of two configurations, either facing the surface as H-down (see Fig. 7 using Method 1 at -1 V \AA^{-1}), or lying flat as H-up (see Fig. 7 using Methods 1 and 2 at 0 V \AA^{-1}). However, it was observed that the water molecule preferred the H-down position towards the metal surface only under the influence of strong electric fields when Method 1 was applied. Conversely, in Method 2, the configurations of the water molecules were more complex, exhibiting both surface-facing and flat positions at different electric fields without following a consistent pattern. These patterns align with previous studies suggesting that varying electric fields significantly affect water molecule orientations and interactions on the metal surface.^{30,39,118} It is noteworthy that in the case of $^*\text{CH}_3\text{CH}_2\text{O}$, the water favored an H-down orientation at -1.0 V \AA^{-1} using Method 1. However, using Method 2, the H-up orientation was found to be the most energetically favorable at the same electric field. Conversely, at -0.4 V \AA^{-1} , the H-up orientation was preferred using Method 1, while the H-down configuration was energetically preferred using Method 2. This difference in geometric preferences can be attributed to the different approaches used in Method 2,

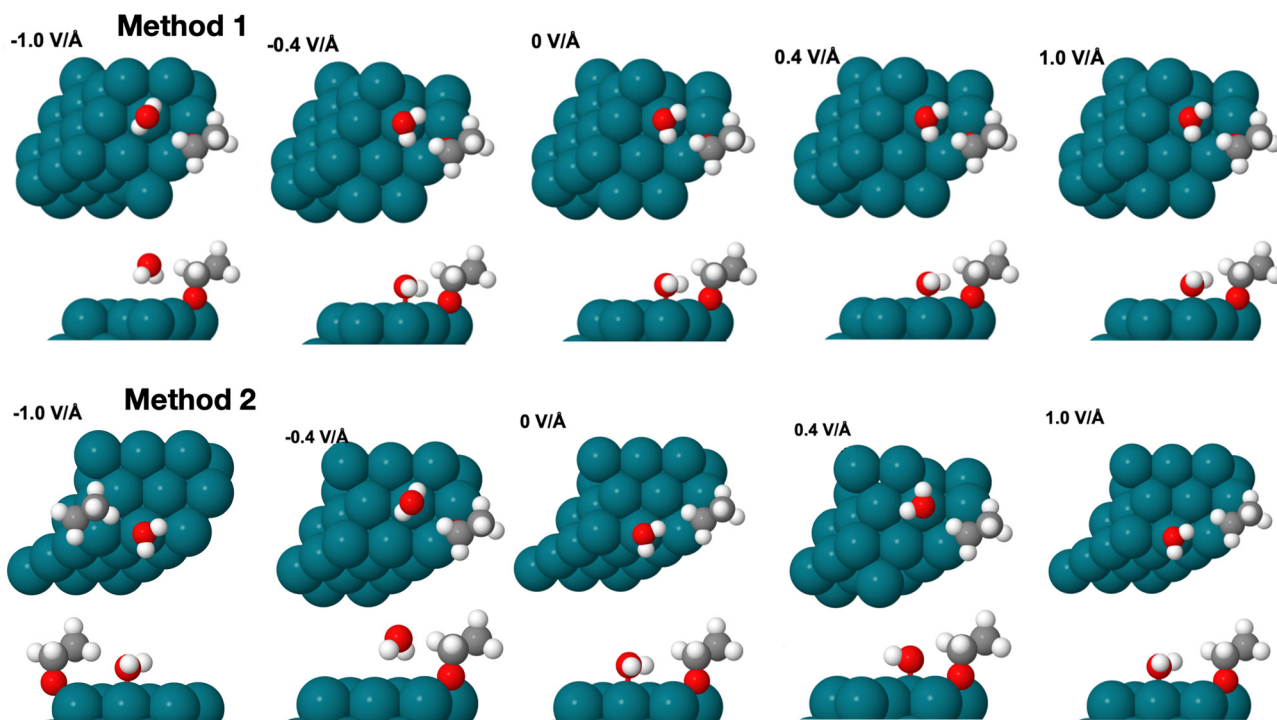


Fig. 7 An example result showing how the optimization method affects the convergence of geometries. Shown are $\text{CH}_3\text{CH}_2\text{O}$ structures in an electric field with water using Methods 1 (top) and 2 (bottom). Different orientations may arise, depending on the solvation approach and field strength. For instance, the H-down water orientation occurred at -1.0 V \AA^{-1} using Method 1, while the H-up water orientation occurred at -1.0 V \AA^{-1} using Method 2. Grey spheres represent carbon atoms, red spheres represent oxygen atoms, white spheres represent hydrogen atoms, and blue spheres represent rhodium atoms.



where both H-up and H-down configurations were initially modeled for geometry optimization and energy calculations at various electric fields. Therefore, the Method 2 configurations shown in Fig. 7 represent the most energetically favorable results of these calculations.

Table 2 also shows that for the ethanol-related intermediates, Methods 1 and 2 yield similar Bader charges under positive electric fields and no electric field conditions. However, under strong negative electric fields at -1.0 V \AA^{-1} , pronounced differences in Bader charges are observed for species such as $^*\text{CH}_3\text{CH}_2\text{OH}$, $^*\text{CH}_2\text{O}$, $^*\text{CH}_2$, $^*\text{CH}$, and $^*\text{CH}_3\text{COOH}$. In these cases, Method 1 tends to favor the H-down configuration of the water molecules, while Method 2 shows a preference for the H-up configuration. This difference in water molecule orientation results in significant Bader charge discrepancies (greater than $0.45 e^-$) between the two methods, underscoring the influence of solvent interactions and molecular orientation on electronic properties.

Hydrogen bond distances at different potentials are also given in Table S3 (ESI[†]). As previously discussed, the differences in the most energetically favorable configurations of the intermediates between Method 1 and Method 2 can be substantial, especially under different external electric fields, mainly due to fluctuations in the orientation of the water molecules (either H-up or H-down). Consequently, these orientation differences affect the hydrogen bonding distances between water molecules and adsorbates. For example, in the case of $\text{CH}_3\text{CH}_2\text{O}$, the interaction between the water molecule and the adsorbate exhibits weak hydrogen bonding, with average bond distances of 2.75 \AA for Method 1 and 2.50 \AA for Method 2, showing notable differences in the most energetically stable configurations between the two methods (Fig. 7). Conversely, there are cases where the most energetically favorable structures remain consistent using both methods. To illustrate, we also provide examples such as $\text{CH}_2\text{CH}_2\text{O}$ and CO , where the interaction between water molecules and adsorbates involves strong hydrogen bonding, with average bond distances of 1.49 \AA for Method 1 and 1.46 \AA for Method 2 in $\text{CH}_2\text{CH}_2\text{O}$, and 1.93 \AA for Method 1 and 1.94 \AA for Method 2 in CO . The most energetically stable geometries for $\text{CH}_2\text{CH}_2\text{O}$ and CO are consistent between Method 1 and Method 2 (see Fig. S12 and S13, ESI[†]). In summary, Methods 1 and 2 may give similar geometries and energies for some species. But our results have also shown that simply using the most stable geometries from potential-free calculations (*i.e.*, Method 1) may not yield the most stable geometries under an applied potential and that the initial geometries may strongly affect the geometry optimization. Care must be taken to ensure that the correct geometries are used for calculations with an electric field.

Fig. 3 shows the adsorption energies in vacuum, while Fig. 6 shows adsorption energies in the presence of water. We also show a comparison of adsorption energies in vacuum and water in Fig. S15 (ESI[†]). The adsorption energies decreased significantly in some cases in the presence of an electric field without a water molecule present, as indicated by the negative slope of

the adsorption energy curves. However, the lowest adsorption energies tended to occur near 0 V \AA^{-1} in the presence of water, while this was not the case with no water molecule present. Adsorption energies tended to increase in water compared to vacuum for several species: $\text{CH}_3\text{CH}_2\text{O}$, CH_3 , and CH_2 , CH . The largest increase in adsorption energy in water compared to vacuum occurred with CH_3 , having an increase of 0.46 eV at 1.0 V \AA^{-1} . The average adsorption energy increases in water *versus* vacuum are 0.14 , 0.13 , 0.08 and 0.08 eV for $\text{CH}_3\text{CH}_2\text{O}$, CH_3 , CH_2 , CH , respectively. However, the adsorption energies in water decreased compared to vacuum for several species: $\text{CH}_3\text{CH}_2\text{OH}$, $\text{CH}_2\text{CH}_2\text{O}$, CH_2O , CH_2CO , CHCO , CO , H , and OH . The average decreases in adsorption energy were -0.13 , -0.16 , -0.10 , -0.12 , -0.29 , -0.16 , -0.01 , and -0.24 eV for $\text{CH}_3\text{CH}_2\text{OH}$, $\text{CH}_2\text{CH}_2\text{O}$, CH_2O , CH_2CO , CHCO , CO , H , and OH , respectively. The largest decrease was -0.42 eV for OH .

In conclusion, in the presence of water, the adsorption of several adsorbates could be significantly affected by an electric field. Water interactions with an adsorbate resulted in adsorption behavior that was significantly different from that in vacuum for many adsorbates. Adsorption energy curves in the presence of water tended to be parabolic, while adsorption energy curves in vacuum tended to be more linear, with positive or negative slopes. Adsorption energies decreased for some species in the presence of water (compared to vacuum calculations) due to the formation of intermolecular hydrogen bonds. Some species were destabilized with water compared to vacuum. In addition, relying solely on vacuum-optimized geometries to guide solvent calculations (Method 1) may not yield the most stable geometries at the applied potential. To ensure that the most stable geometries are obtained, several initial geometries should be considered (Method 2). This effect of water on adsorption energies can have an impact on reactivity, which will be discussed further in the next section.

3.6 Further electronic analysis

To gain deeper understanding of how electric fields affect the electronic interactions between adsorbates and the Rh surface, we also investigated the density of states (DOS) and charge difference density (CDD) for selected species from the three different groups which are identified in Sections 3.1 and 3.3. These species include $\text{CH}_3\text{CH}_2\text{OH}$ (decreasing adsorption energy with increasing electric field), CHCO (increasing adsorption energy with increasing electric field), and CH_2CO (adsorption energies increasing with increasing or decreasing electric field), as shown in Fig. 3. Fig. 8 details the DOS analysis for $\text{CH}_3\text{CH}_2\text{OH}$, with additional data for CH_2CO and CHCO in Fig. S8 (ESI[†]). Under an electric field orbitals can change. For instance, Fig. 8 shows $\text{CH}_3\text{CH}_2\text{OH}$ has increased hybridization with the orbitals of the Rh surface with increasing potential, as the $\text{CH}_3\text{CH}_2\text{OH}$ levels shift up in energy (closer to the Fermi level). See for instance the orbital around -12 eV (as well as other orbitals) at -1 V \AA^{-1} shift to high levels with increasing potential. In contrast, the orbitals for H_2O appear to decrease with increasing electric field. In the case of CH_2CO , orbitals move slightly closer to the Fermi level with increasing potential.



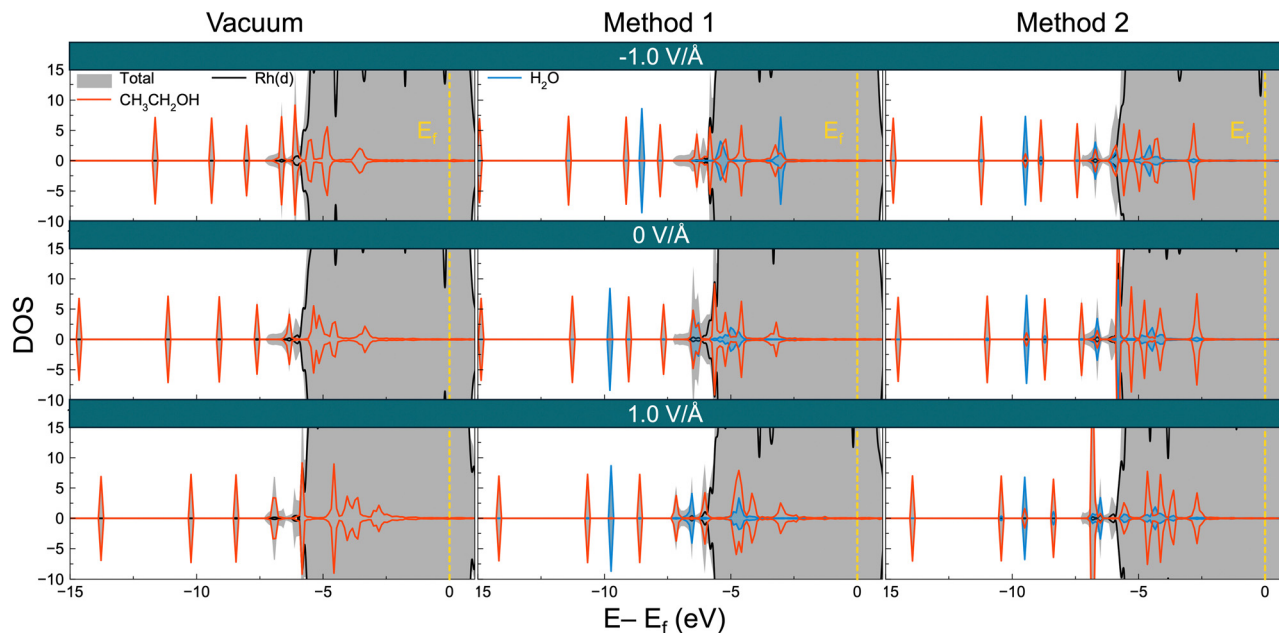


Fig. 8 Density of states (DOS) analysis of $\text{CH}_3\text{CH}_2\text{OH}$ using different solvation methods and applied fields. The figures in each row represent the DOS of the adsorbed $\text{CH}_3\text{CH}_2\text{OH}$ in a negative electric field ($-1 \text{ V } \text{\AA}^{-1}$), no electric field ($0 \text{ V } \text{\AA}^{-1}$), and in a positive electric field ($1 \text{ V } \text{\AA}^{-1}$). The Fermi level corresponds to 0 eV .

On the other hand CHCO orbitals have a less discernible pattern. For all three molecules interactions between the water molecule and adsorbate are apparent, with such interactions missing in the vacuum calculations.

Fig. 9 shows CDD plots for $\text{CH}_3\text{CH}_2\text{OH}$, while Fig. S9 (ESI[†]) shows CDD plots for CH_2CO and CHCO. In vacuum $\text{CH}_3\text{CH}_2\text{OH}$ has the most stable adsorption energy at positive potentials. Fig. 9 shows that in vacuum there are more electron density changes between the adsorbate and surface at $1 \text{ V } \text{\AA}^{-1}$, compared to the other CDD plots under vacuum, and thus is consistent with the adsorption energy behavior. Unsurprising, when water is present there are significant changes in electron density in the vicinity of the water molecule, as the water molecule interacts with both the surface and the adsorbate. Fig. 6 indicates that Method 2 geometries are the most stable for $\text{CH}_3\text{CH}_2\text{OH}$, and that adsorption energies are most stable near 0 eV , increasing under any electric field. This is consistent with the CDD plots. The CDD plots of $\text{CH}_3\text{CH}_2\text{OH}$ using Method 2 have the largest electron density changes at $0 \text{ V } \text{\AA}^{-1}$. See for instance the region around the water molecule for these pronounced changes. Method 1 has the smallest electron density changes at $-1 \text{ V } \text{\AA}^{-1}$, and noticeably the water molecule is farthest from the Rh surface. Similar patterns can be seen for the other molecules. CHCO, for instance, has the most stable adsorption energy in vacuum at negative potentials, and the greatest electron density changes in vacuum are seen at $-1 \text{ V } \text{\AA}^{-1}$ for CHCO (see Fig. S9, ESI[†]).

3.7 Effect of an electric field and water on reactivity

A combination of co-adsorbed water and electric field can significantly affect the surface reactions for EOR, as shown in

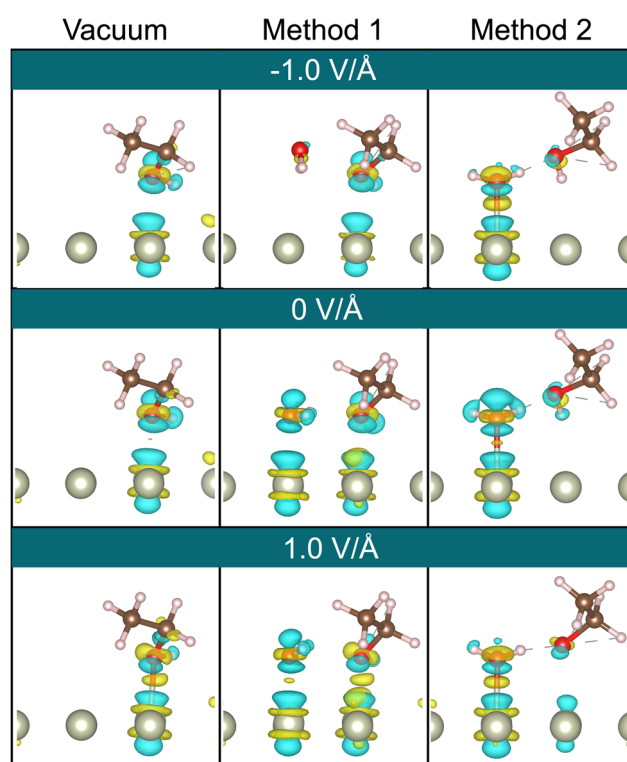


Fig. 9 Charge density difference analysis of $\text{CH}_3\text{CH}_2\text{OH}$ on the Rh(111) surface in the presence and the absence of an electric field. The yellow or blue areas represent a gain or loss of electrons. The isosurface level of the differential charge densities of $\text{CH}_3\text{CH}_2\text{OH}$ is $0.004 \text{ e bohr}^{-3}$.

Fig. 10 and 11. For C–C bond cleavage, the choice of initial geometries can have far-reaching effects on reaction energies.



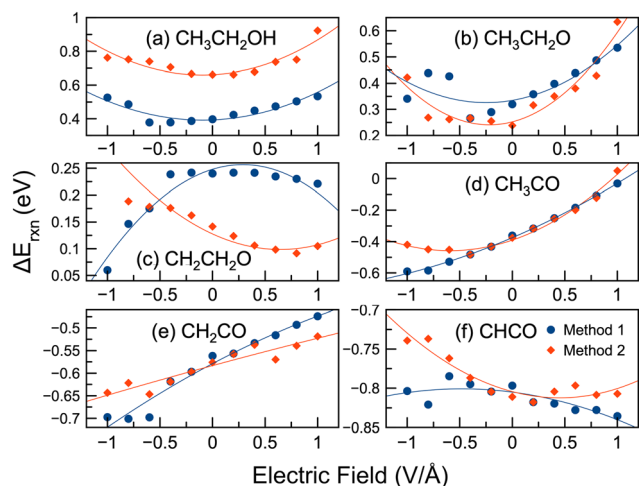


Fig. 10 Reaction energies for C–C bond breaking in the presence of an electric field and water phase. Method 1 and Method 2 were used for generating initial geometries. Reactions involved: (a) $\text{CH}_3\text{CH}_2\text{OH} \rightarrow \text{CH}_3 + \text{CH}_2\text{OH}$; (b) $\text{CH}_3\text{CH}_2\text{O} \rightarrow \text{CH}_3 + \text{CH}_2\text{O}$; (c) $\text{CH}_2\text{CH}_2\text{O} \rightarrow \text{CH}_2 + \text{CH}_2\text{O}$; (d) $\text{CH}_3\text{CO} \rightarrow \text{CH}_3 + \text{CO}$; (e) $\text{CH}_2\text{CO} \rightarrow \text{CH}_2 + \text{CO}$; (f) $\text{CHCO} \rightarrow \text{CH} + \text{CO}$.

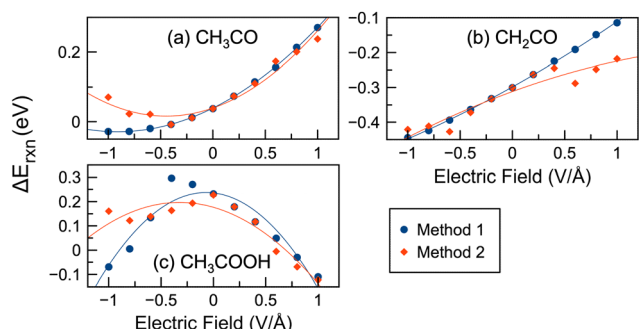


Fig. 11 Reaction energies for C–H bond breaking and C–O bond formation in the presence of an electric field and water phase. Method 1 and Method 2 were used for generating initial geometries. Reactions involved: (a) $\text{CH}_3\text{CO} \rightarrow \text{CH}_2\text{CO} + \text{H}$; (b) $\text{CH}_2\text{CO} \rightarrow \text{CHCO} + \text{H}$; (c) $\text{CH}_3\text{CO} + \text{OH} \rightarrow \text{CH}_3\text{COOH}$.

Fig. 10 shows that for many reactions Methods 1 and 2 give very different reaction-potential plots. The reaction energy plot for the C–C scission of $\text{CH}_3\text{CH}_2\text{OH}$ had a parabolic shape, but the two methods give energies ~ 0.3 eV apart. Interestingly, Method 2, which gives the most stable structures, had more exothermic reaction energies than Method 1. This suggests that simply using Method 1, or the most stable potential-free geometry, may underestimate C–C scission in ethanol. The plot for C–C scission of $\text{CH}_3\text{CH}_2\text{O}$ was also parabolic, but the difference between the two methods was 0.04 eV on average. The plots for CH_3CO and CH_2CO had positive slopes, except for CH_3CO using Method 2. However, the differences between Method 1 and Method 2 for the C–C cleavage of these two reactants were small, averaging 0.03 eV for CH_3CO and 0.002 eV for CH_2CO . An interesting phenomenon from our work shows that the reaction plots for $\text{CH}_2\text{CH}_2\text{O}$ and CHCO had very different shapes depending on the initial choice of geometry

for the water molecules. Method 1 gave concave parabolic curves, while Method 2 gave convex parabolic curves. This discrepancy in reaction energies between the two methods can be explained by the different geometries and adsorption behaviors of the reactants and products. For example, Fig. S14 (ESI[†]) illustrates the geometries for structures during C–C bond cleavage of $\text{CH}_2\text{CH}_2\text{O}$. Different final geometries of products and reactants occurred using the different solvation approaches (Methods 1 and 2). Accordingly, different reaction energy patterns emerged for $\text{CH}_2\text{CH}_2\text{O}$ and CHCO . Therefore, our results again highlight the importance of the initial geometry choice, especially when multiple molecules or solvent molecule(s) may be present.

For C–H bond cleavage (Fig. 11), the effect of an electric field was very similar for the vacuum and water cases. The reaction energies increased with increasing potential, although CH_3CO showed a slight increase at very negative potentials when using Method 2. The reaction energies between Method 1 and 2 had an increase of up to 0.10 eV for the cleavage of the CH_3CO C–H bond at $-1.0 \text{ V } \text{\AA}^{-1}$, and a decrease of 0.10 eV at $1.0 \text{ V } \text{\AA}^{-1}$ for the cleavage of the CH_2CO C–H bond. The average reaction energy changes were 0.01 eV for C–H scission in CH_3CO and -0.03 eV for C–H scission in CH_2CO . Methods 1 and 2 gave similar C–H scission reaction energies except at low potentials with CH_3CO and high potentials with CH_2CO . For C–O bond formation with water, the reaction energy curves were parabolic (concave) as in the vacuum calculations. Negative electric fields decreased the reaction energy by up to 0.30 eV, while positive electric fields decreased the reaction energy by up to 0.34 eV.

Fig. 4, 5, 10 and 11 show the reaction energies in vacuum and with water. We also show a comparison of these energies in Fig. S16 and S17 (ESI[†]). Comparing the reaction energies with water (Method 2) to the vacuum calculations, the reaction energies of C–C bond cleavage in $\text{CH}_3\text{CH}_2\text{O}$, CH_3CO , and C–H bond cleavage in CH_3CO and CH_2CO were on average lower in water than in vacuum. The average energy decreases of these reactions were -0.10 , -0.04 , -0.14 , and -0.18 eV, respectively. The largest energy decrease was -0.27 eV for the C–H bond cleavage in CH_2CO . However, the reaction energies of C–C bond scission of $\text{CH}_3\text{CH}_2\text{OH}$, $\text{CH}_2\text{CH}_2\text{O}$, CH_2CO , and CHCO became more endothermic in water compared to vacuum by 0.26, 0.14, 0.04, and 0.21 eV, respectively. The largest energy difference was 0.48 eV for $\text{CH}_3\text{CH}_2\text{OH}$. The C–O bond formation energies were more endothermic in water than in vacuum, with an average difference of 0.28 eV. These changes in reaction energy are due to strong adsorption of reactant intermediates (e.g., $^*\text{CH}_2\text{CH}_2\text{O}$, $^*\text{CH}_2\text{CO}$) or weak adsorption of product intermediates (e.g., $^*\text{CH}_2$, $^*\text{CH}$). The results are consistent with our previous solvation work,⁴⁵ in that explicit water solvation favors C–C scission of $\text{CH}_3\text{CH}_2\text{O}$, CH_3CO ; and C–H scission in CH_3CO and CH_2CO . However, our current and previous work also showed that water inhibited the C–C scission of $\text{CH}_2\text{CH}_2\text{O}$, CH_2CO and CHCO and C–O bond formation.

In summary, our results show that the application of an external electric field significantly affects the energies involved in the cleavage of C–C and C–H bonds with co-adsorbed water.



This effect varies between reactions occurring under vacuum conditions and those with water, as shown in our results (as shown in Fig. 4, 5 and 10, 11). The choice of initial geometric configurations (Methods 1 and 2) yielded different results. In particular, C–C bond cleavage in molecules such as $\text{CH}_3\text{CH}_2\text{OH}$, $\text{CH}_3\text{CH}_2\text{O}$, CH_3CO , along with C–H bond cleavage in CH_3CO and CH_2CO , showed more favorable (exothermic) reaction energies in the presence of water compared to vacuum scenarios. Conversely, certain reactions involving C–C bond cleavage (as in $\text{CH}_2\text{CH}_2\text{O}$, CH_2CO , and CHCO) and C–O bond formation showed less favorable (more endothermic) results in water. In addition, the influence of electric fields on the reaction energy changes for most of the C–C bond cleavages studied typically showed a parabolic trend, with negative electric fields more likely to promote C–H bond cleavages and C–C cleavages in CH_2CO . We do note that previous work⁴⁶ examined C–C cleavage under potential, although only cleavage of CH_3CO was studied using implicit solvation. In this work reaction energies only changed slightly with potential, possibly due to the use of implicit solvation and a different metal (Pd).

3.8 Comparing EOR reactivity in different electrochemical environments

The breaking of C–C bonds is a necessary step for the complete oxidation of ethanol. In this work, we have modeled C–C scission in three different environments: vacuum with no electric field, electric field only (vacuum), and electric field with water. We compare the reaction energies in these different environments for C–C scission in Fig. 12. We show that C–C scission is predominantly exothermic for reactions involving

CH_xCO (*i.e.*, late reaction species after many C–H scission steps), whereas it is predominantly endothermic for reactions involving $\text{CH}_3\text{CH}_2\text{OH}$, $\text{CH}_3\text{CH}_2\text{O}$, and $\text{CH}_2\text{CH}_2\text{O}$ (*i.e.*, early reaction species with few C–H scission steps). This agrees with previous DFT and experimental work where CH_xCO species have been implicated as key species for C–C splitting.^{76,77,103–105} Notably, the presence of water and an electric field does not change the fact that C–C scission is easiest through late species (CH_xCO).

Our results show that at no applied potential ($0 \text{ V } \text{\AA}^{-1}$), C–C scission was easiest for CHCO (*i.e.* the lowest reaction energy), followed by CH_2CO and then CH_3CO , regardless of whether water was present. The reaction energies decrease at negative potentials for CH_3CO and CH_2CO (positive slope), but increase for CHCO (negative slope), again regardless of whether water is present. Reaction energy changes for C–C scission of CHCO between $-1 \text{ V } \text{\AA}^{-1}$ and $1 \text{ V } \text{\AA}^{-1}$ were 0.05 eV (vacuum), 0.03 eV (Method 1), and 0.07 eV (Method 2). These small numbers indicate that the applied field had only a small effect on the C–C scission of CHCO . On the other hand, the reaction energy changes for C–C scission of CH_3CO between $-1 \text{ V } \text{\AA}^{-1}$ and $1 \text{ V } \text{\AA}^{-1}$ were 0.46 eV (vacuum), 0.56 eV (Method 1), and 0.47 eV (Method 2). Reaction energy changes for C–C scission of CH_2CO between $-1 \text{ V } \text{\AA}^{-1}$ and $1 \text{ V } \text{\AA}^{-1}$ were 0.22 eV (vacuum), 0.22 eV (Method 1), and 0.12 eV (Method 2). Clearly, the electric field has a much larger effect on the scission of CH_3CO and CH_2CO . We note that while CHCO has the most exothermic reaction energies, at very low negative potentials the scission of CH_2CO can become competitive with CHCO scission due to close reaction energies. For example, the reaction energies for CH_2CO scission at $-1 \text{ V } \text{\AA}^{-1}$ are -0.74 eV (vacuum) and -0.64 eV (Method 2), while the reaction energies for CHCO scission at $-1 \text{ V } \text{\AA}^{-1}$ are -0.95 eV (vacuum) and -0.74 eV (Method 2). Our results thus show that negative potentials can open new reaction pathways for C–C scission involving CH_2CO , and that the competition becomes more pronounced in the presence of water. This conclusion could not be reached without considering the electrochemical environment present during EOR.

We further examined the reaction data to understand and rationalize the observed trends. The reaction energy at a potential \vec{F} can be expanded as in the following series:¹¹⁹

$$\Delta E(\vec{F})_{\text{rxn}} \approx \Delta E(\vec{F} = 0)_{\text{rxn}} - \Delta \vec{\mu}_{\text{rxn}} \cdot \vec{F} - \frac{1}{2} \Delta \alpha_{\text{rxn}} \vec{F}^2. \quad (6)$$

Here $\Delta E(\vec{F} = 0)_{\text{rxn}}$ is the reaction energy with no electric field applied, $\Delta \vec{\mu}_{\text{rxn}}$ is a vector of the reaction dipole moment (difference in dipole moments between products and reactants), and $\Delta \alpha_{\text{rxn}}$ is the reaction polarizability (difference in polarizability between products and reactants). Fitting the reaction plots (Fig. 12) yields the reaction dipole moments and polarizabilities, and these values are given in Table 3. According to eqn (6), the changes in dipole moments between products and reactants ($\Delta \vec{\mu}_{\text{rxn}}$) are the key to how much an electric field affects the reaction energies. As noted above, an electric field has little effect on the C–C cleavage of CHCO

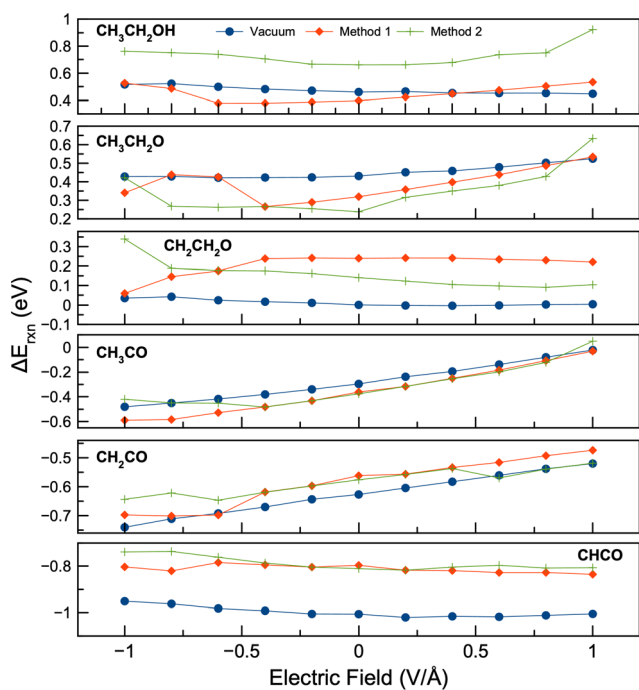


Fig. 12 A comparison of C–C bond breaking reaction energies using the various approaches of this study. Indicated are the reactants for C–C scission, with reaction energies at different potentials.



Table 3 The reaction dipole moments (in units of eV \AA^{-1}) and polarizabilities (in units of $\text{eV \AA}^2 \text{V}^{-2}$) for C–C scission reactions as calculated from a Taylor series expansion of the reaction energies as a function of electric field (eqn (7)). Indicated are the reactants for which C–C scission occurs

	Vacuum		Method 1		Method 2	
	$ \Delta\vec{\mu}_{\text{rxn}} $	$\Delta\alpha_{\text{rxn}}$	$ \Delta\vec{\mu}_{\text{rxn}} $	$\Delta\alpha_{\text{rxn}}$	$ \Delta\vec{\mu}_{\text{rxn}} $	$\Delta\alpha_{\text{rxn}}$
*CH ₃ CH ₂ OH	0.0376	-0.0414	-0.026	-0.2772	-0.0333	-0.346
*CH ₃ CH ₂ O	-0.0475	-0.0878	-0.0696	-0.2804	-0.1038	-0.4754
*CH ₂ CH ₂ O	0.0206	-0.0398	-0.0602	0.208	0.0901	-0.1394
*CH ₃ CO	-0.2314	-0.0842	-0.287	-0.1164	-0.2269	-0.3832
*CH ₂ CO	-0.109	0.0076	-0.1229	0.0356	-0.063	0.005
*CHCO	0.0288	-0.0672	0.0173	0.0358	0.0354	-0.0786

(see Fig. 12). In fact, the $\Delta\vec{\mu}_{\text{rxn}}$ values for CHCO are all small ($<0.04 \text{ eV \AA}^{-1}$), as shown in Table 3. Similarly, the difference between the product and reactant dipole moments from Table 1 for CHCO C–C scission is $\approx 0 \text{ eV \AA}^{-1}$. Thus, the total change in dipole moment between products and reactants for CHCO scission is close to zero, and thus an electric field has little effect on the reaction energy for CHCO scission. This is not the case for CH₂CO and CH₃CO, where the changes in dipole moments (using values from Table 1 and also using data from Table 3) are all negative, indicating that an electric field would and does have a measurable effect on the reaction energies. Notably, we observe that changes in dipole moments occur regardless of whether water is present or not.

We do acknowledge the limitations of our results. All our calculations have essentially been static calculations, focused on reaction energies. This approach has been used previously to study EOR.^{45,46} Activation energies would provide more insight into the nature of these reaction steps. However, such calculations are time-consuming and complicated, especially when incorporating solvation and electric fields. Such calculations may be the topic of future work. Scaling relationships do indicate that often activation energies are proportional to reaction energies, and linear scaling relationships have been applied to the study of C–C breaking of ethanol over various metals (albeit with no electric fields or solvent molecules present).^{77,103} Related work³⁷ on methane steam reforming over Ni showed linear scaling relationships changed only slightly in the presence of both positive or negative electric fields. Thus, we expect lower reaction energies to correspond to lower activation energies. We also point out that modeling the dynamic nature of electrochemical reactions is an ongoing area of research. For instance, kinetic Monte Carlo calculations have been used to simulate electrocatalytic systems as they change over time^{120,121} or ethanol decomposition.⁷⁶ Certainly applying such methods to study the EOR would provide valuable insights, and again may be the topic of future work.

4 Conclusions

Our results showed that electric fields significantly modify the oxidation process. Under vacuum conditions the adsorption energy differences between results using fields of 1 V \AA^{-1} and

-1 V \AA^{-1} were up to 1 eV, with an average change of 0.44 eV. Positive electric fields generally reduced the adsorption energies for most species except CH₂CO, CHCO, CO, and H atoms, while negative electric fields tended to favor the adsorption of CHCO and CO species only. Negative fields reduced reaction energies for some C–C and C–H bond cleavage reactions by up to 0.5 eV, but also enhanced C–O bond formation. Positive fields had little impact on lowering reaction energies, occasionally increasing them. These results correlate well with experimental findings that negative potentials lead to ethanol reduction. The study also aligned with previous findings that positive electric fields lower adsorption energies for species with positive dipole moments (*i.e.* CH₃CH₂OH, CH₃CH₂O, CH₂CH₂O, CH₂OH, CH₂O, CH₃CO, CH₃, CH₂, and CH), while negative electric fields produce a similar effect for molecules with negative dipole moments (*i.e.* CHCO and CO). Additionally, for species whose dipole moments are approximately zero, adsorption energies increase in both positive and negative electric fields (*i.e.* CH₂CO and H).

We also examined how electric fields and the presence of water impact ethanol oxidation on Rh(111). We employed two methods to incorporate water molecules into our calculations. In Method 1 the initial geometries were taken from converged structures involving no electric fields. In Method 2 four different initial geometries were used at each electric field strength. Method 2 is a more robust process to explore possible structures, but also more time-consuming. These approaches yielded different geometries and energy profiles for several species, emphasizing the importance of a comprehensive exploration of possible geometries in electrochemical systems. The presence of water altered the adsorption energy trends, causing them to generally become more parabolic under an electric field. It also enhanced C–C and C–H bond cleavage by up to -0.27 eV but could inhibit C–O bond formation by about 0.28 eV. Electric fields, especially negative fields, favor the cleavage of C–H and specific C–C bonds such as CH₂CO, while most C–C bond cleavages become more parabolic under an electric field in the presence of water. We also found that C–C bond cleavage is most likely to occur in CHCO, followed by CH₂CO and CH₃CO. Although electric fields have minimal effect on C–C bond cleavage in CHCO, they significantly affect CH₂CO C–C cleavage. Under strong electric fields C–C scission through CHCO and CH₂CO become competitive, demonstrating the potential of electric fields to manipulate chemical reaction pathways. Overall, our study illuminates the significance of electric fields and solvent molecules in electrochemical ethanol oxidation, showcasing their impact on adsorption processes and reaction pathways.

Data availability

Data for this article are included in the main text and ESI.† Simulation files are available at: <https://github.com/Deskins-group/Structure-Files/tree/master/Ethanol%20Oxidation%20-%20Potential>.



Conflicts of interest

There are no conflicts to declare.

Acknowledgements

This work was supported by the National Science Foundation under Grant No. 1705830. We also acknowledge the computational resources provided by Worcester Polytechnic Institute.

Notes and references

- S. Q. Song, W. J. Zhou, Z. H. Zhou, L. H. Jiang, G. Q. Sun, Q. Xin, V. Leontidis, S. Kontou and P. Tsiakaras, *Int. J. Hydrogen Energy*, 2005, **30**, 995–1001.
- Y. Wang, S. Zou and W. B. Cai, *Catalysts*, 2015, **5**, 1507–1534.
- F. Barbir and T. Gómez, *Int. J. Hydrogen Energy*, 1997, **22**, 1027–1037.
- X. Li and I. Sabir, *Int. J. Hydrogen Energy*, 2005, **30**, 359–371.
- A. S. Aricè, P. Cretì, P. L. Antonucci and V. Antonucci, *Electrochem. Solid-State Lett.*, 1998, **1**, 66–68.
- M. Z. Kamarudin, S. K. Kamarudin, M. S. Masdar and W. R. Daud, *Int. J. Hydrogen Energy*, 2013, **38**, 9438–9453.
- M. Li, A. Kowal, K. Sasaki, N. Marinkovic, D. Su, E. Korach, P. Liu and R. R. Adzic, *Electrochim. Acta*, 2010, **55**, 4331–4338.
- U. B. Demirci, *J. Power Sources*, 2007, **173**, 11–18.
- Y. M. Choi and P. Liu, *J. Am. Chem. Soc.*, 2009, **131**, 13054–13061.
- M. Li, W. Guo, R. Jiang, L. Zhao, X. Lu, H. Zhu, D. Fu and H. Shan, *J. Phys. Chem. C*, 2010, **114**, 21493–21503.
- R. Jiang, W. Guo, M. Li, H. Zhu, L. Zhao, X. Lu and H. Shan, *J. Mol. Catal. A: Chem.*, 2011, **344**, 99–110.
- J. Bai, D. Liu, J. Yang and Y. Chen, *ChemSusChem*, 2019, **12**, 2117–2132.
- L. Yaqoob, T. Noor and N. Iqbal, *RSC Adv.*, 2021, **11**, 16768–16804.
- K. Schwarz and R. Sundararaman, *Surf. Sci. Rep.*, 2020, **75**, 100492.
- R. Sundararaman, D. Vigil-Fowler and K. Schwarz, *Chem. Rev.*, 2022, **122**, 10651–10674.
- J. A. Herron, Y. Morikawa and M. Mavrikakis, *Proc. Natl. Acad. Sci. U. S. A.*, 2016, **113**, E4937–E4945.
- A. A. Peterson, F. Abild-Pedersen, F. Studt, J. Rossmeisl and J. K. Nørskov, *Energy Environ. Sci.*, 2010, **3**, 1311–1315.
- J. Cheng and M. Sprik, *Phys. Chem. Chem. Phys.*, 2012, **14**, 11245–11267.
- J. Cheng, X. Liu, J. VandeVondele, M. Sulpizi and M. Sprik, *Acc. Chem. Res.*, 2014, **47**, 3522–3529.
- X. Zhao and Y. Liu, *J. Am. Chem. Soc.*, 2021, **143**, 9423–9428.
- S. Yu, Z. Levell, Z. Jiang, X. Zhao and Y. Liu, *J. Am. Chem. Soc.*, 2023, **145**, 25352–25356.
- J. Neugebauer and M. Scheffler, *Phys. Rev. B: Condens. Matter Mater. Phys.*, 1992, **46**, 16067–16080.
- J. Rossmeisl, J. K. Nørskov, C. D. Taylor, M. J. Janik and M. Neurock, *J. Phys. Chem. B*, 2006, **110**, 21833–21839.
- S. R. Kelly, C. Kirk, K. Chan and J. K. Nørskov, *J. Phys. Chem. C*, 2020, **124**, 14581–14591.
- C.-H. Yeh, T. M. L. Pham, S. Nachimuthu and J.-C. Jiang, *ACS Catal.*, 2019, **9**, 8230–8242.
- X. Z. Jiang, M. Feng, W. Zeng and K. H. Luo, *Proc. Combust. Inst.*, 2019, **37**, 5525–5535.
- X. Z. Jiang and K. H. Luo, *Proc. Combust. Inst.*, 2021, **38**, 6605–6613.
- Y. Pan, X. Wang, W. Zhang, L. Tang, Z. Mu, C. Liu, B. Tian, M. Fei, Y. Sun and H. Su, *et al.*, *Nat. Commun.*, 2022, **13**, 3063.
- F. Che, J. T. Gray, S. Ha, N. Kruse, S. L. Scott and J. S. McEwen, *ACS Catal.*, 2018, **8**, 5153–5174.
- F. Che, J. T. Gray, S. Ha and J. S. McEwen, *J. Catal.*, 2015, **332**, 187–200.
- G. S. Karlberg, J. Rossmeisl and J. K. Nørskov, *Phys. Chem. Chem. Phys.*, 2007, **9**, 5158–5161.
- V. V. Welborn, L. Ruiz Pestana and T. Head-Gordon, *Nat. Catal.*, 2018, **1**, 649–655.
- P. Besalu-Sala, M. Sola, J. M. Luis and M. Torrent-Sucarrat, *ACS Catal.*, 2021, **11**, 14467–14479.
- Z. Zhang, C. Li, X. Du, Y. Zhu, L. Huang, K. Yang, J. Zhao, C. Liang, Q. Yu, S. Li, X. Liu and Y. Zhai, *Chem. Eng. J.*, 2023, **452**, 139098.
- J. Haruyama, T. Ikeshoji and M. Otani, *Phys. Rev. Mater.*, 2018, **2**, 095801.
- K.-Y. Yeh and M. J. Janik, *J. Comput. Chem.*, 2011, **32**, 3399–3408.
- F. Che, J. T. Gray, S. Ha and J. S. McEwen, *ACS Catal.*, 2017, **7**, 551–562.
- J. T. Gray, F. Che, J.-S. McEwen and S. Ha, *Appl. Catal., B*, 2020, **260**, 118132.
- A. Estejab, R. A. García Cárcamo and R. B. Getman, *Phys. Chem. Chem. Phys.*, 2022, **24**, 4251–4261.
- F. Che, R. Zhang, A. J. Hensley, S. Ha and J. S. McEwen, *Phys. Chem. Chem. Phys.*, 2014, **16**, 2399–2410.
- F. Che, S. Ha and J.-S. McEwen, *Appl. Catal., B*, 2016, **195**, 77–89.
- W. Zhou, W. Zhou, L. Yang and Z. Jia, *Fuel*, 2023, **350**, 128759.
- B. Schweitzer, S. N. Steinmann and C. Michel, *Phys. Chem. Chem. Phys.*, 2019, **21**, 5368–5377.
- G. H. Gu, B. Schweitzer, C. Michel, S. N. Steinmann, P. Sautet and D. G. Vlachos, *J. Phys. Chem. C*, 2017, **121**, 21510–21519.
- Y. Mei and N. A. Deskins, *Phys. Chem. Chem. Phys.*, 2021, **23**, 16180–16192.
- Y. Guo, B. Li, S. Shen, L. Luo, G. Wang and J. Zhang, *ACS Appl. Mater. Interfaces*, 2021, **13**, 16602–16610.
- M. Li, A. Kowal, K. Sasaki, N. Marinkovic, D. Su, E. Korach, P. Liu and R. R. Adzic, *Electrochim. Acta*, 2010, **55**, 4331–4338.
- H. Idriss, *Platinum Met. Rev.*, 2004, **48**, 105–115.
- G. Yang, A. I. Frenkel, D. Su and X. Teng, *ChemCatChem*, 2016, **8**, 2876–2880.



- 50 A. Resta, J. Blomquist, J. Gustafson, H. Karhu, A. Mikkelsen, E. Lundgren, P. Uvdal and J. N. Andersen, *Surf. Sci.*, 2006, **600**, 5136–5141.
- 51 M. Mavrikakis, J. Rempel, J. Greeley, L. B. Hansen, J. K. Nørskov and J. Rempel, *J. Chem. Phys.*, 2002, **117**, 6730–6741.
- 52 C. Michel, F. Auneau, F. Delbecq and P. Sautet, *ACS Catal.*, 2011, **1**, 1430–1440.
- 53 M. M. Yang, X. H. Bao and W. X. Li, *J. Phys. Chem. C*, 2007, **111**, 7403–7410.
- 54 A. Y. Lozovoi, A. Alavi, J. Kohanoff and R. M. Lynden-Bell, *J. Chem. Phys.*, 2001, **115**, 1661–1669.
- 55 C. D. Taylor, S. A. Wasileski, J. S. Filhol and M. Neurock, *Phys. Rev. B: Condens. Matter Mater. Phys.*, 2006, **73**, 165402.
- 56 A. Y. Lozovoi and A. Alavi, *Phys. Rev. B: Condens. Matter Mater. Phys.*, 2003, **68**, 245416.
- 57 Y. He, X. Y. Wei, C. T. Chan and J. G. Che, *Phys. Rev. B: Condens. Matter Mater. Phys.*, 2005, **71**, 45401.
- 58 J. S. Filhol and M. Neurock, *Angew. Chem., Int. Ed.*, 2006, **45**, 402–406.
- 59 J. K. Nørskov, J. Rossmeisl, A. Logadottir, L. Lindqvist, J. R. Kitchin, T. Bligaard and H. Jónsson, *J. Phys. Chem. B*, 2004, **108**, 17886–17892.
- 60 G. Rostamikia, A. J. Mendoza, M. A. Hickner and M. J. Janik, *J. Power Sources*, 2011, **196**, 9228–9237.
- 61 X. K. Gu and E. Nikolla, *J. Phys. Chem. C*, 2015, **119**, 26980–26988.
- 62 H.-F. Wang and Z.-P. Liu, *J. Phys. Chem. C*, 2009, **113**, 17502–17508.
- 63 J. R. Pliego and J. M. Riveros, *J. Phys. Chem. A*, 2001, **105**, 7241–7247.
- 64 G. Kresse and J. Hafner, *Phys. Rev. B: Condens. Matter Mater. Phys.*, 1994, **49**, 14251–14269.
- 65 G. Kresse and J. Hafner, *Phys. Rev. B: Condens. Matter Mater. Phys.*, 1993, **47**, 558–561.
- 66 G. Kresse and J. Furthmüller, *Phys. Rev. B: Condens. Matter Mater. Phys.*, 1996, **54**, 11169–11186.
- 67 G. Kresse and J. Furthmüller, *Comput. Mater. Sci.*, 1996, **6**, 15–50.
- 68 P. E. Blöchl, *Phys. Rev. B: Condens. Matter Mater. Phys.*, 1994, **50**, 17953–17979.
- 69 G. Kresse and D. Joubert, *Phys. Rev. B: Condens. Matter Mater. Phys.*, 1999, **59**, 1758–1775.
- 70 J. P. Perdew, K. Burke and M. Ernzerhof, *Phys. Rev. Lett.*, 1996, **77**, 3865–3868.
- 71 M. Methfessel and A. T. Paxton, *Phys. Rev. B: Condens. Matter Mater. Phys.*, 1989, **40**, 3616–3621.
- 72 G. Henkelman, A. Arnaldsson and H. Jónsson, *Comput. Mater. Sci.*, 2006, **36**, 354–360.
- 73 E. Sanville, S. D. Kenny, R. Smith and G. Henkelman, *J. Comput. Chem.*, 2007, **28**, 899–908.
- 74 W. Tang, E. Sanville and G. Henkelman, *J. Phys.: Condens. Matter*, 2009, **21**, 84204.
- 75 M. L. Williams, *Occup. Environ. Med.*, 1996, **53**, 504.
- 76 Y. Choi and P. Liu, *Catal. Today*, 2011, **165**, 64–70.
- 77 P. Ferrin, D. Simonetti, S. Kandoi, E. Kunkes, J. A. Dumesic, J. K. Nørskov and M. Mavrikakis, *J. Am. Chem. Soc.*, 2009, **131**, 5809–5815.
- 78 H.-F. Wang and Z.-P. Liu, *J. Am. Chem. Soc.*, 2008, **130**, 10996–11004.
- 79 Q. Meng, Y. Shen, J. Xu and J. Gong, *Chin. J. Catal.*, 2012, **33**, 407–415.
- 80 M. Shetty, M. A. Ardagh, Y. Pang, O. A. Abdelrahman and P. J. Dauenhauer, *ACS Catal.*, 2020, **10**, 12867–12880.
- 81 A. Alizadeh Sahraei and F. Larachi, *Appl. Surf. Sci.*, 2021, **576**, 151899.
- 82 P. Deshlahra, E. E. Wolf and W. F. Schneider, *J. Phys. Chem. A*, 2009, **113**, 4125–4133.
- 83 P. J. Feibelman, *Phys. Rev. B: Condens. Matter Mater. Phys.*, 2001, **64**, 125403.
- 84 R. Alcalá, M. Mavrikakis and J. A. Dumesic, *J. Catal.*, 2003, **218**, 178–190.
- 85 F. Colmati, G. Tremiliosi-Filho, E. R. Gonzalez, A. Berná, E. Herrero and J. M. Feliu, *Phys. Chem. Chem. Phys.*, 2009, **11**, 9114–9123.
- 86 B. Miao, Z.-P. Wu, H. Xu, M. Zhang, Y. Chen and L. Wang, *Comput. Mater. Sci.*, 2019, **156**, 175–186.
- 87 B. Miao, Z. Wu, H. Xu, M. Zhang, Y. Chen and L. Wang, *Chem. Phys. Lett.*, 2017, **688**, 92–97.
- 88 E. A. Monyoncho, S. N. Steinmann, P. Sautet, E. A. Baranova and C. Michel, *Electrochim. Acta*, 2018, **274**, 274–278.
- 89 A. O. Pereira and C. R. Miranda, *Appl. Surf. Sci.*, 2014, **288**, 564–571.
- 90 Q. Zhang and A. Asthagiri, *Catal. Today*, 2019, **323**, 35–43.
- 91 D. Loffreda, C. Michel, F. Delbecq and P. Sautet, *J. Catal.*, 2013, **308**, 374–385.
- 92 C. J. Bodenschatz, S. Sarupria and R. B. Getman, *J. Phys. Chem. C*, 2015, **119**, 13642–13651.
- 93 T. Xie, S. Sarupria and R. B. Getman, *Mol. Simul.*, 2017, **43**, 370–378.
- 94 T. Xie, C. J. Bodenschatz and R. B. Getman, *React. Chem. Eng.*, 2019, **4**, 383–392.
- 95 X. Zhang, R. S. DeFever, S. Sarupria and R. B. Getman, *J. Chem. Inf. Model.*, 2019, **59**, 2190–2198.
- 96 J. Zhang, X. M. Cao, P. Hu, Z. Zhong, A. Borgna and P. Wu, *J. Phys. Chem. C*, 2011, **115**, 22429–22437.
- 97 C. T. Yang, B. C. Wood, V. R. Bhethanabotla and B. Joseph, *Phys. Chem. Chem. Phys.*, 2015, **17**, 25379–25392.
- 98 J. S. Filhol and M. L. Doublet, *J. Phys. Chem. C*, 2014, **118**, 19023–19031.
- 99 E. Masumian, S. M. Hashemianzadeh and A. Nowroozi, *Phys. Lett. Sect. A: Gen. At. Solid State Phys.*, 2014, **378**, 2549–2552.
- 100 Y. Dong, J. Dang, W. Wang, S. Yin and Y. Wang, *ACS Appl. Mater. Interfaces*, 2018, **10**, 39624–39630.
- 101 S. Aboud and J. Wilcox, *J. Phys. Chem. C*, 2010, **114**, 10978–10985.
- 102 G. Hu, Z. Wu and D. E. Jiang, *J. Mater. Chem. A*, 2018, **6**, 7532–7537.
- 103 J. E. Sutton and D. G. Vlachos, *Ind. Eng. Chem. Res.*, 2015, **54**, 4213–4225.



- 104 D. Cantane, W. Ambrosio, M. Chatenet and F. Lima, *J. Electroanal. Chem.*, 2012, **681**, 56–65.
- 105 Q. He, S. Mukerjee, B. Shyam, D. Ramaker, S. Parres-Esclapez, M. Illán-Gómez and A. Bueno-López, *J. Power Sources*, 2009, **193**, 408–415.
- 106 F. Zhang, D. Zhou, Z. Zhang, M. Zhou and Q. Wang, *RSC Adv.*, 2015, **5**, 91829–91835.
- 107 J. Zhang, J. Ye, Q. Fan, Y. Jiang, Y. Zhu, H. Li, Z. Cao, Q. Kuang, J. Cheng, J. Zheng and Z. Xie, *J. Am. Chem. Soc.*, 2018, **140**, 11232–11240.
- 108 H. Li, J. Ye, X. Li, J. Zhang, Y. Zhu, Z. Zhou, Y. Xue, Y. Jiang, Z. Xie and L. Zheng, *J. Mater. Chem. A*, 2019, **7**, 26266–26271.
- 109 G. Yang, L. Farsi, Y. Mei, X. Xu, A. Li, N. A. Deskins and X. Teng, *J. Am. Chem. Soc.*, 2019, **141**, 9444–9447.
- 110 J. J. Varghese and S. H. Mushrif, *React. Chem. Eng.*, 2019, **4**, 165–206.
- 111 M. Saleheen and A. Heyden, *ACS Catal.*, 2018, **8**, 2188–2194.
- 112 C. D. Taylor and M. Neurock, *Curr. Opin. Solid State Mater. Sci.*, 2005, **9**, 49–65.
- 113 B. N. Zope, D. D. Hibbitts, M. Neurock and R. J. Davis, *Science*, 2010, **330**, 74–78.
- 114 C. Hartnig, J. Grimminger and E. Spohr, *Electrochim. Acta*, 2007, **52**, 2236–2243.
- 115 M. Faheem and A. Heyden, *J. Chem. Theory Comput.*, 2014, **10**, 3354–3368.
- 116 H. H. Heenen, J. A. Gauthier, H. H. Kristoffersen, T. Ludwig and K. Chan, *J. Chem. Phys.*, 2020, **152**, 144703.
- 117 J. A. Herron, Y. Morikawa and M. Mavrikakis, *Proc. Natl. Acad. Sci. U. S. A.*, 2016, **113**, E4937–E4945.
- 118 J.-S. Filhol and M.-L. Bocquet, *Chem. Phys. Lett.*, 2007, **438**, 203–207.
- 119 M. Wan, H. Yue, J. Notarangelo, H. Liu and F. Che, *JACS Au*, 2022, **2**, 1338–1349.
- 120 C. H. Lee, S. Pahari, N. Sitapure, M. A. Barteau and J. S.-I. Kwon, *ACS Catal.*, 2023, **13**, 8336–8346.
- 121 Y. Luo, Y. Guan, G. Liu, Y. Wang, J. Li and L. Ricardez-Sandoval, *ACS Catal.*, 2024, **14**, 2696–2708.

